nature communications

Article

https://doi.org/10.1038/s41467-025-65390-y

Surface mechanics and compressive stress impact mammalian follicle development

Received: 1 May 2025

Accepted: 15 October 2025

Published online: 31 October 2025

Check for updates

Arikta Biswas[1], Yuting Lou[1,2], Boon Heng Ng[1], Kosei Tomida[1], Sukhada Darpe[1], Kim Whye Leong[1], Zihao Wu[1], Thong Beng Lu[3], Xiang Teng[1], Yusuke Toyama[1,4], Isabelle Bonne[3,5] & Chii Jou Chan[1,4]

The maturation of functional eggs in ovaries is essential for successful reproduction in mammals. Despite its biological and clinical importance, the underlying mechanisms regulating folliculogenesis remain enigmatic. Here, using murine ovaries, we report that the theca cells surrounding secondary follicles play a critical role in regulating follicle development through mechanical signalling. Using biophysical approaches, we found that the contractile theca cells exert significant compressive stress to the follicular interior through active assembly of fibronectin. Manipulation of compressive stress by targeting theca cell contractility, basement membrane integrity or intrafollicular pressure leads to changes in follicle size and mechanics, granulosa cell YAP signalling and oocyte-granulosa cell communications. Transcriptomics and quantitative immunofluorescence reveal that compressive stress impacts functional follicle growth through regulating the balance between granulosa cell proliferation and death that drives tissue pressure homeostasis. Altogether, our study uncovers unique mechanical functions of theca cells and provides quantitative evidence of the role of compressive stress in regulating mammalian folliculogenesis.

The maturation of functional oocytes within the ovarian follicles is undoubtedly one of the most significant developmental events in reproductive biology. The growth of follicles, or folliculogenesis, is essential for ensuring successful reproduction and regulating hormones for female sexual characteristics and early pregnancy[1,2]. Folliculogenesis begins with the primordial follicle, where a single oocyte is surrounded by a layer of granulosa cells (GCs) and basement membrane (BM). Upon activation, they develop into primary follicles characterised by the formation of columnar GCs, which surround the oocyte with a glycoprotein shell of zona pellucida (ZP). The oocyte and the GCs maintain bi-directional communications through the transzonal projections (TZPs). The follicles then develop into secondary follicles with the formation of multi-layered GCs and an external layer of spindle-shaped theca cells (TCs). As the follicles grow, a large fluid-filled lumen forms within the GC layers, which ultimately leads to follicle rupture and release of the oocyte, a process known as ovulation.

While past molecular genetics studies have identified genes that are critical for folliculogenesis[3,4], the underlying mechanisms regulating follicle growth remain enigmatic. In recent years, evidence has emerged showing that the ovary is a mechanically responsive organ[5] and that mechanical signalling can impact follicle dynamics and development[6,7]. For example, it is known that follicle growth in 3D culture is highly sensitive to the surrounding matrix stiffness[8,9], and fragmentation of ovaries can disrupt the Hippo signalling pathway and promote follicle growth[10–12]. Mechanical stress imposed by the extracellular matrix (ECM) controls primordial follicle dormancy[13], while

[1]Mechanobiology Institute, National University of Singapore, Singapore, Singapore. [2]Multiscale Research Institute for Complex Systems and State Key Laboratory of Molecular Engineering of Polymers, Fudan University, Shanghai, China. [3]Electron Microscopy Unit, Microscopy Core Facility Cluster, Yong Loo Lin School of Medicine, National University of Singapore, Singapore, Singapore. [4]Department of Biological Sciences, National University of Singapore, Singapore, Singapore. [5]Department of Microbiology & Immunology, Immunology Translational Research Programme, Yong Loo Lin School of Medicine, National University of Singapore, Singapore, Singapore. e-mail: dbschii@nus.edu.sg

changes in ECM stiffness during ovarian ageing has been implicated in poor oocyte quality[14] and anovulation[15]. These studies highlight the role of compressive stress in regulating ovary functions which has been implicated in other contexts such as spheroid growth[16], tumour progression[17], diseases[18] and organ development[19,20]. Yet, fundamental questions remain as to how mechanical stress is generated and sustained within the follicles, and how it orchestrates follicle morphogenesis and oocyte maturation.

A recent study revealed that the intrafollicular environment is characterised by distinct mechanical properties of TCs and GCs[21]. The TCs are indispensable for folliculogenesis as they are involved in the production of steroid hormones for ovulation[22,23]. Abnormalities in TC steroidogenic functions can lead to polycystic ovary syndrome (PCOS)[24,25], a prominent cause of female infertility[26], and hyperthecosis[27], a condition usually affecting postmenopausal women and causing virilization[28]. TCs have also been implicated in early menopause in reproductive-aged women[29]. Yet, apart from hormonal regulation, the structural and mechanical functions of TCs remain largely unknown. In this study, we investigated the mechanical interactions between TCs and granulosa cells during secondary follicle development. Using in vitro and ex vivo approaches, combined with quantitative imaging, biophysical tools, molecular and physical perturbations, we revealed the roles of follicle surface mechanics and compressive stress in regulating follicular mechanics, granulosa cell signalling and follicle growth.

Results

Ovarian theca cells are highly contractile

While the structural and steroidogenic properties of TCs around the large follicles have been well studied[30,31], those surrounding the early secondary follicles (120-250 μm) have not been characterised so far. Hence, we first examined the steroidogenic profiles of TCs in young murine ovaries (3-4 weeks), and found that while steroidogenic markers like CYP11A1 and CYP17A1 (Supplementary Fig. 1A) only appear in the large lumen-filled antral follicles, nuclear steroid co-regulatory factor COUPTF-II (NR2F2) and vascular cell adhesion molecule (VCAM1) are expressed in theca cells across all follicle stages (Supplementary Fig. 1B, C). On isolating secondary follicles from the ovaries, we observed that the expression patterns of these markers are preserved (Supplementary Fig. 1B–D), suggesting that the TC characteristics are retained ex vivo.

Given the highly stretched and spindle-like morphology of TCs, we hypothesise that, in addition to their role in steroidogenesis, the theca cells may have mechanical functions in exerting contractile forces around the follicles. To this end, we immuno-stained ovarian tissue slices and isolated secondary follicles targeting phosphorylated myosin light chain 2 (pMLC), which has been reported to be a good proxy for actomyosin contractility[32]. We found that the TCs express high amounts of pMLC compared to the minimal levels observed in the GCs, both in situ (Fig. 1A, B) and ex vivo (Fig. 1C, D), suggesting that the TCs are indeed contractile. Of note, TCs are devoid of adherens junctional proteins such as Neural cadherin (N-Cad) and Epithelial cadherin (E-Cad) (Supplementary Fig. 1E), consistent with recent literature[33,34]. This suggests that these cells exhibit characteristics that are less epithelial in nature and more closely resemble mesenchymal and fibroblast-like properties. Inhibition of actomyosin contractility with blebbistatin (Blebb) led to a decrease in TCs' pMLC expression while hyperactivation of contractility with lysophosphatidic acid (LPA) did not increase the TCs' pMLC expression further, both in situ (Supplementary Fig. 2A, B) and ex vivo (Supplementary Fig. 2C, D). We observed an increase in TCs' pMLC expressions with larger follicles ex vivo (Fig. 1E). However, direct tension measurement by micropipette aspiration (MPA) revealed no significant change in TC shell surface tension with follicle growth (Fig. 1F), suggesting that the secondary follicles maintained their surface tension during development. While the oocyte cortex expressed some levels of pMLC expression, its intensity did not change upon actomyosin perturbations (Supplementary Fig. 2D, E), suggesting that the impact of the drugs is mainly specific to the outer contractile TCs.

We next measured the surface tension of individual TCs in the secondary follicles using atomic force microscopy (AFM, Supplementary Methods). We found that the TCs exhibit an effective surface tension of 0.51 ± 0.20 mN/m (Fig. 1G). Follicles treated with Blebb and LPA showed a significant decrease and increase in the measured TC surface tension, respectively (Fig. 1G). Since quantifying TC tension by AFM can be model-dependent, we directly measured single TC tension using MPA[35]. Indeed, we observed a decrease or increase in TC tension upon Blebb and LPA treatment, respectively (Fig. 1H). Notably, the relative change of TC tension between control and perturbations is similar to that measured by AFM. These data are also consistent with cell rounding or stretching associated with surface tension release or increase (Supplementary Fig. 2F, G).

We then isolated primary TCs from bulk ovaries[36] to check if the high contractility is an intrinsic feature of the TCs. Consistent with previous reports which show alkaline phosphatase (ALP) positive staining on the TCs in pre-ovulatory follicles[37], we noted ALP expression at the periphery of follicles in ovarian slices (Supplementary Fig. 3A). Isolated TCs expressed more ALP and appeared more elongated and spread out on 2D substrates compared to the smaller and more cuboidal GCs that are ALP-negative (Supplementary Fig. 3B–D). Using traction force microscopy, we found that the TCs exert significantly higher traction stresses than the GCs (Fig. 1I), which is correlated with their spread area (Supplementary Fig. 3E), indicating they are indeed intrinsically more contractile than the GCs.

Altogether, based on our findings in situ, ex vivo and in vitro, we conclude that the TCs are highly contractile, which can potentially regulate follicle development through mechanical signalling.

Theca cells exert compressive stress to modulate follicle mechanics and pressure

We hypothesised that the contractile TCs may exert compressive stress to regulate follicle size and functions. Since quantifying compressive stress in situ is challenging, we resorted to an in vitro approach where we allowed secondary follicles to attach to similar-sized deformable gelatin beads and tracked the bead-follicle pairs for two days by timelapse imaging (Supplementary Movie 1). We observed that the TCs migrated from the follicles to the beads and uniformly enwrapped the beads within 12 hours. Using dextran-based osmotic compression assay[38], we found that the beads have an average bulk modulus (a measure of compressibility) of 19.4 ± 6.3 kPa (Fig. 2A, Methods). This information, combined with the tracking of changes in bead volume during TC enwrapment (Fig. 2B, left), allowed us to uniquely determine the compressive stress exerted by the TCs on the beads to be ~2 kPa. The compressive stress decreased or increased significantly with Blebb or LPA treatment (Fig. 2B, right), respectively, suggesting that the compressive stress originated from TC contractility.

We next considered whether perturbing TC contractility directly impacts follicle size. On tracking every follicle, we observed that transient inhibition of contractility with Blebb (Fig. 2C, left) or Y27632 (Fig. 2C, right) for 30 mins led to an increase in follicle volume. Washing out of both inhibitors over similar timescales led to a restoration of follicle volume, suggesting that the volume regulation by TC-mediated contractility is fast, global, and reversible. Using a similar dextran-based compression assay, we determined the effective bulk modulus (K) of secondary follicles to be ~27.5 ± 13.4 kPa (Fig. 2D). This, together with the measured volumetric strain of ~0.1 upon perturbation (Fig. 2C), allowed us to infer the compressive stress exerted by TCs on secondary follicles to be ~2.75 kPa, consistent with that measured using the bead-follicle assay.

https://doi.org/10.1038/s41467-025-65390-y

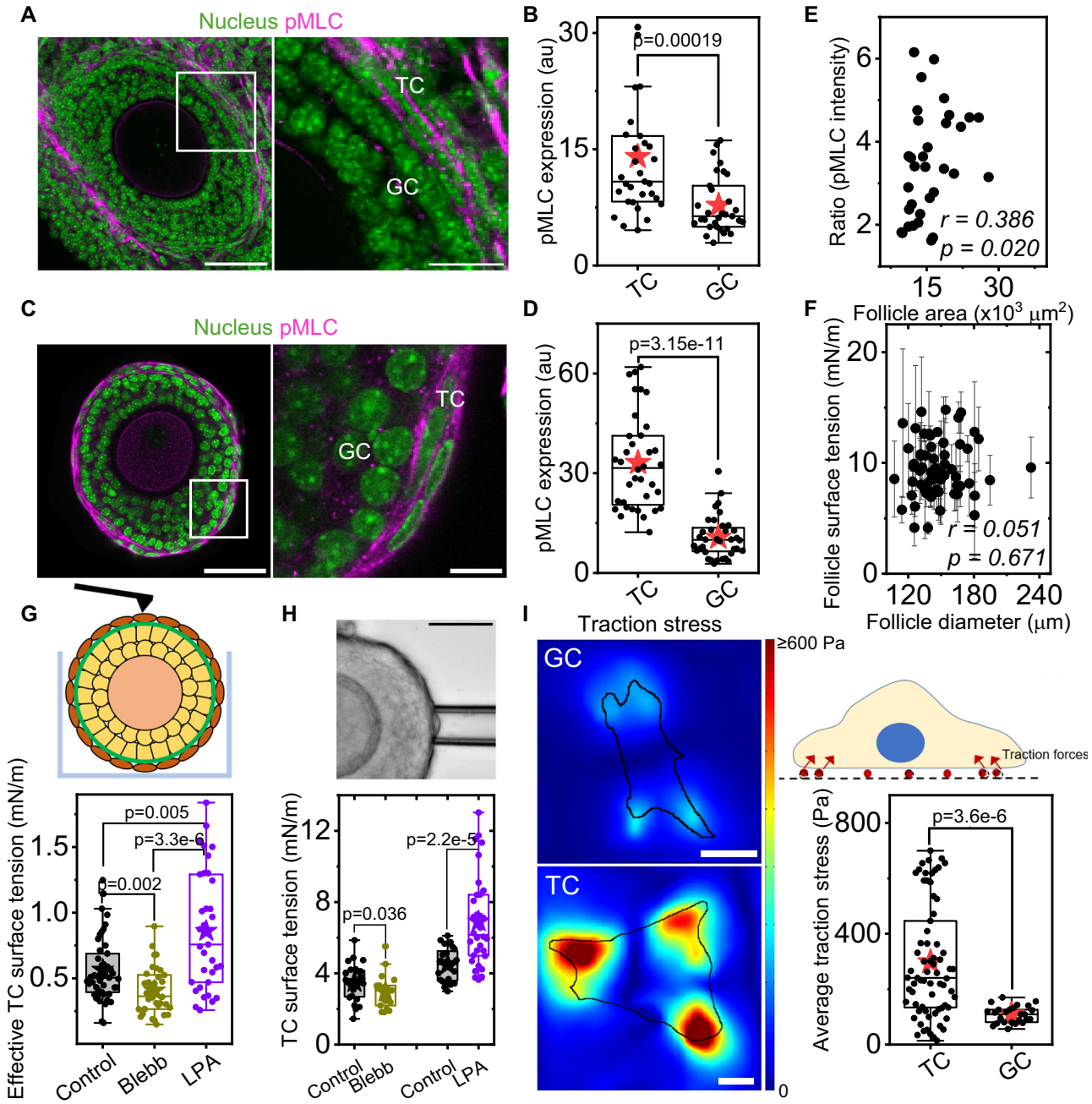

Fig. 1 | Ovarian theca cells are highly contractile. A Left: Representative image of an ovarian tissue slice labelled with DAPI (nucleus, green) and immuno-stained with phosphorylated-myosin light chain (pMLC, magenta). Scale bar: 50 μm. Right: inset shows the zoomed-in region marked in white. Scale bar: 20 μm. **B** Boxplots of pMLC intensities in TCs and GCs in situ. $n = 31$ follicles. **C** Left: Representative image of an isolated secondary follicle labelled with DAPI (green) and immuno-stained with pMLC (magenta). Scale bar: 50 μm. Right: inset shows the zoomed-in region marked in white. Scale bar: 10 μm. **D** Boxplots of pMLC intensities in TCs and GCs ex vivo. $n = 36$ follicles. **E** Scatter plot of pMLC intensity ratios as a function of follicle size ex vivo. The Pearson correlation coefficient (r) and significance (p, two-tailed test) are noted in the plot. $n = 36$ follicles. **F** Plot of follicle surface tension as a function of follicle size. Symbols and error bars represent the average and standard deviation of three measurements in each follicle respectively. The Pearson correlation coefficient (r) and significance (p, two-tailed test) are noted in the plot. $n = 65$ follicles. **G** Top: Schematic of AFM-based indentation on a follicle in a microwell to measure TC surface tension. Bottom: Boxplots of effective TC surface tension in control, Blebb, and LPA-treated samples. $n = 45$ (control), 35 (Blebb, LPA) follicles. **H** Top: Representative image of a secondary follicle during micropipette aspiration. Scale bar: 50 μm. Bottom: Boxplots of average TC tension in control, Blebb, and LPA-treated samples. $n = 24$ (control), 19 (Blebb); $n = 28$ (control), 32 (LPA) follicles. **I** Left: Representative traction stress maps for isolated GCs and TCs in vitro. Outline of the cells are marked in black. Scale bar: 10 μm. Right top: Schematic of traction force microscopy. Right bottom: Box plot of average traction stress (per cluster) for TCs and GCs. $n = 70$ clusters (TC) and 25 clusters (GC) from 25 cells. Boxplots show the mean (star), median (center line), quartiles (box limits), and 1.5x interquartile range (whiskers). Significance was determined by a two-tailed Mann–Whitney U test (pairwise) in (**B**, **D**, **G**, **H**, **I**). All data are from at least four biological replicates. Source data are provided as a Source Data file.

https://doi.org/10.1038/s41467-025-65390-y

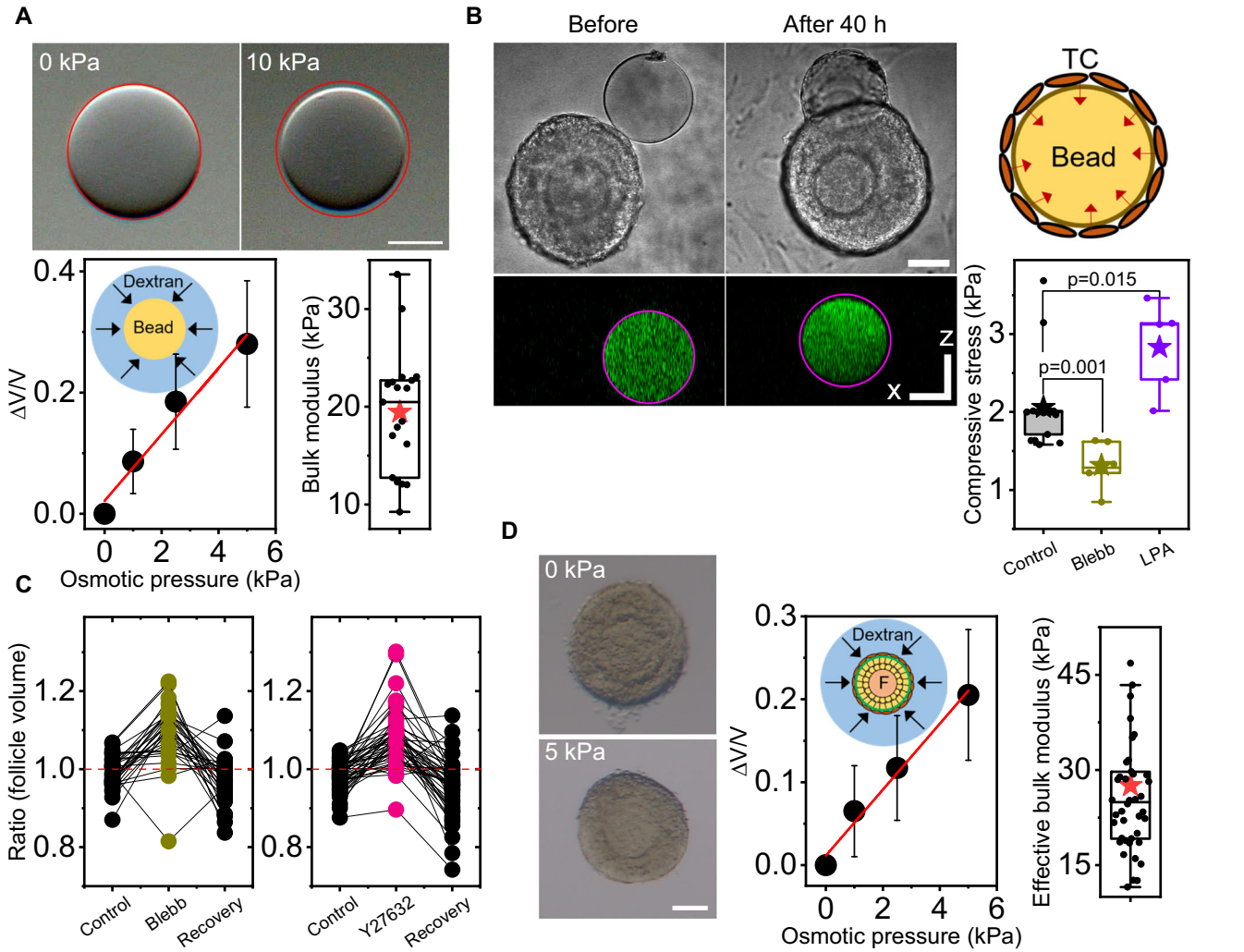

Fig. 2 | Theca cells generate compressive stress to regulate follicle size. A Top: Representative images of a bead under different osmotic stress. The outline of the initial bead boundary is marked in red. Scale bar: 50 μm. Bottom left: Plot of relative change of bead volume against osmotic stress (black symbols) and the linear fit (red line). Data is plotted as mean ± standard deviation (SD). Bottom right: Box plot of measured bulk modulus of beads. $n = 20$ beads. **B** Left: Representative images of a bead before and after TC enwrapment – brightfield (top) and orthogonal view (bottom). The outline of the initial bead boundary is marked in magenta. Scale bar: 50 μm. Right: Boxplots of compressive stress measured in control, Blebb, and LPA-treated TCs. $n = 17$ (control), 6 (Blebb, LPA) bead-follicle pairs. **C** Boxplots of follicle volume change upon perturbations of contractility (left: Blebb; right: Y27632) and washout (recovery). $n = 31$ (Blebb), 48 (Y27632) follicles. **D** Left: Representative images of a secondary follicle under different osmotic pressures. Scale bar: 50 μm. Mid: Plot of relative change in follicle volume against osmotic stress (black symbols) and the linear fit (red line). Data is plotted as mean ± SD. Right: Box plot of measured bulk modulus of secondary follicles. $n = 42$ follicles. Significance was determined by a two-tailed Mann–Whitney U test (pairwise) in (**B**). Boxplots show the mean (star), median (center line), quartiles (box limits), and 1.5x interquartile range (whiskers). All data are from at least four biological replicates. Source data are provided as a Source Data file.

To investigate if changes in follicle volume by TC-mediated compressive stress affects intrafollicular pressure and bulk mechanics, we performed AFM indentations on secondary follicles under various perturbations, using large spherical probes (Fig. 3A). We found that while LPA treatment did not change the effective tissue elasticity (Fig. 3B and Supplementary Information) and effective pressure (Fig. 3D) as compared to that of the controls, blebbistatin treatment led to a significant decrease in both parameters. Furthermore, we observed a large hysteresis between the approach and retraction curves in Blebb-treated follicles (Fig. 3C), indicating that the release of compressive stress from TC relaxation leads to increased stress dissipation and potential change in tissue viscosity. To confirm this, we fitted our AFM data to a Maxwellian viscoelasticity model (see Supplementary information) to extract the apparent viscosity of the follicles. We found that Blebb treatment indeed led to a decrease in apparent follicle viscosity (Supplementary Fig. 4A), consistent with high stress dissipative behaviour. Finally, we observed that Blebb treatment led to a significant reduction in the follicle bulk modulus (Supplementary Fig. 4B) and an overall increase in total interstitial gap area (Fig. 3E, F and Supplementary Fig. 4C), consistent with the notion that a more 'porous-like' tissue can be more compressible and incurs greater stress dissipation.

To further validate the role of TC contractility on intrafollicular pressure, we performed laser ablations by making a point cut at the follicle periphery, followed by tracking of tissue outflow. Following ablation, we observed a rapid displacement of GCs towards the ablation site (Fig. 3G, Supplementary Movie 2). By quantifying the GC flow near the cut region (local parallel velocity) in various conditions, we observed a significant attenuation of GC flow upon Blebb treatment while LPA led to increased GC outflow compared to the controls (Fig. 3H). Taken together, our data confirms that Blebb or LPA treatment led to reduced or increased intrafollicular pressure, respectively.

https://doi.org/10.1038/s41467-025-65390-y

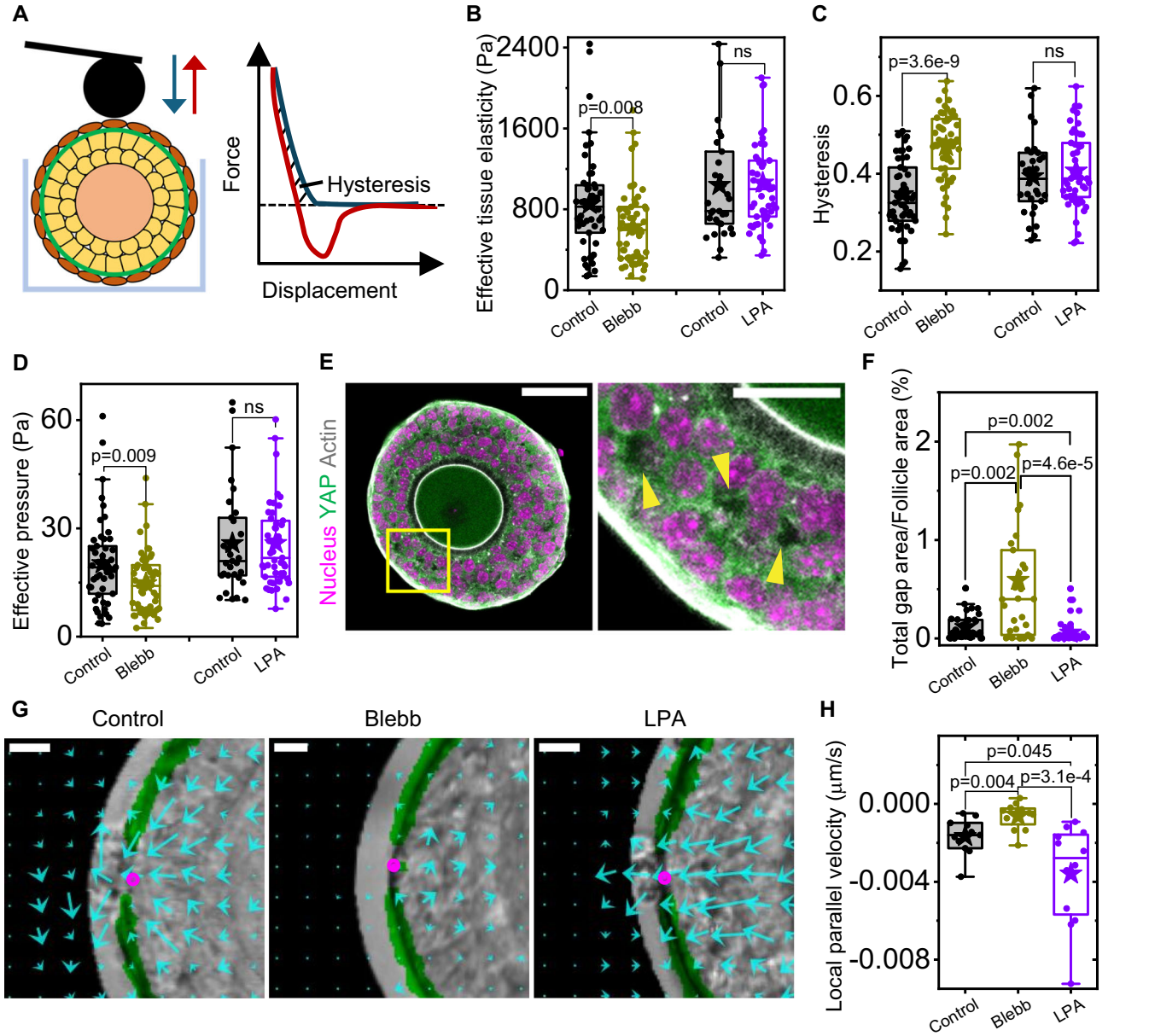

Fig. 3 | Reduced compressive stress leads to decreased intrafollicular pressure and apparent follicle elasticity. A–D Schematic of AFM approach to measure follicle mechanical properties from the approach (blue) and retraction curve (red) (**A**), showing how this yields the effective follicle elasticity (**B**), hysteresis (**C**), and effective pressure (**D**) in various conditions. $n = 51$ (control), 55 (Blebb); n = 31 (control), 51 (LPA) follicles. **E** Left: Representative image of an isolated follicle labelled with DAPI (nucleus, magenta), Phalloidin (actin, grey), and immuno-stained with YAP (green). Scale bar: 50 μm. Right: Zoomed-in image of the yellow box marked on the left. Yellow arrowheads demarcate interstitial gaps. Scale bar: 20 μm. **F** Boxplots of the ratios of total interstitial gaps to follicle area for follicles in various conditions. $n = 34$ (control), 31 (Blebb), 32 (LPA) follicles. **G** Zoomed-in representative displacement vector maps overlaid on CNA35 (green) marked follicles (brightfield) in control, Blebb, and LPA treatments; ablation site is marked by magenta circles. Scale bar: 20 μm. **H** Boxplots of local parallel velocity in the three conditions. $n = 11$ (control), 12 (Blebb, LPA) follicles. Significance was determined by two-tailed Mann–Whitney U test (pairwise) in **B**–**D**, **F**, **H**. ns: $p > 0.05$. Boxplots show the mean (star), median (center line), quartiles (box limits), and 1.5x interquartile range (whiskers). All data are from at least four biological replicates. Source data are provided as a Source Data file.

Finally, LPA led to only a slight further decrease in interstitial gap area (Fig. 3E, F), suggesting that the follicles in their native state are already tightly packed and are not susceptible to further compression, consistent with the lack of a change in compressibility (Supplementary Fig. 4B), follicle volume (Supplementary Fig. 4D) and mechanics (Fig. 3B–D and Supplementary Fig. 4A, B).

Theca cell contractility mediates fibronectin expression

To gain structural insights on how forces are transmitted by the TCs, we immuno-stained for fibronectin (FN) and found abundant FN expression at the theca layers compared to the GCs, both in tissue slices (Fig. 4A, B) and in isolated follicles (Supplementary Fig. 5A). The FN expression increases with follicle development, particularly in isolated follicles (Fig. 4B, right; Supplementary Fig. 5A, right). Interestingly, while the BM has been reported to be enriched with FN in past studies[39], we found the FN layer to be physically separated from the collagen matrix at the BM, as shown by localisation studies (Fig. 4C). In addition, ultrastructural studies using scanning electron microscopy revealed a distinct matrix-like layer separating the basal TCs from the BM (Fig. 4D

https://doi.org/10.1038/s41467-025-65390-y

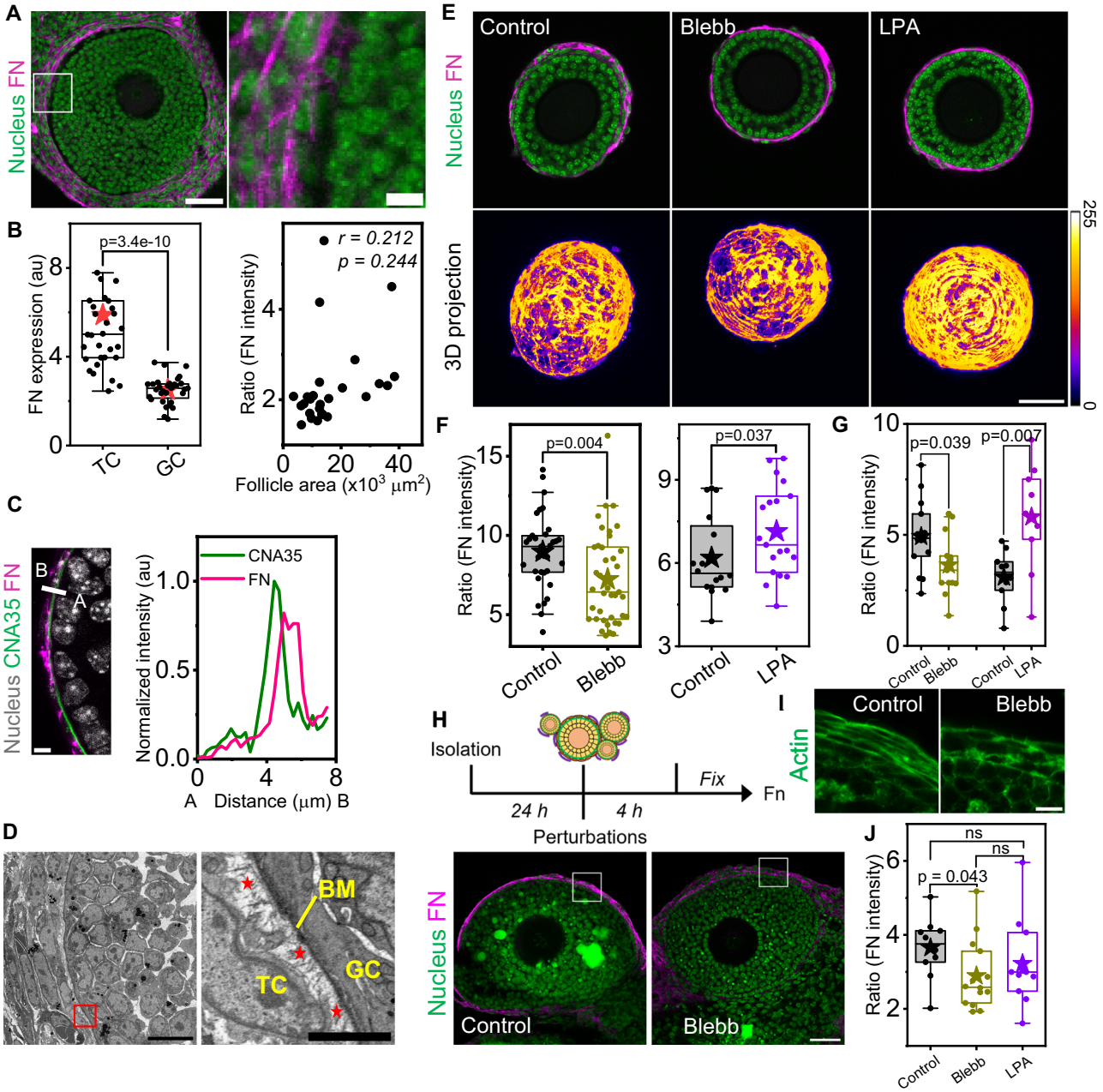

Fig. 4 | Theca cell contractility regulates fibronectin expression. A Left: Representative image of an ovarian slice labelled with DAPI (green) and immunostained with FN (magenta). Scale bar: 50 μm. Right: Zoomed-in region of the marked white box. Scale bar: 5 μm. **B** Left: Boxplots of FN intensity in TCs and GCs in situ. Right: Plot of ratio(FN intensity) at the TC shell against follicle size. The Pearson correlation coefficient (*r*) and significance (*p*, two-tailed test) is noted in the plot. *n* = 32 follicles. **C** Left: Zoomed-in section of a follicle immuno-stained with FN (magenta) and stained with DAPI (grey) and CNA35 (green). Scale bar: 10 μm. Right: Intensity profile for the line scan marked in white (left image). **D** Left: Representative SEM image of a section of a follicle. Right: Zoomed-in section of the red box marked on left. Red asterisks indicate the fibronectin-rich matrix between the BM and the basal TCs. Scale bars: 10 and 2 μm respectively. **E** Representative images of control, Blebb, and LPA-treated follicles labelled with nucleus (green) and fibronectin (magenta), at the equatorial z-plane (top), with corresponding colour-coded 3D projections (bottom). Colour bar represents the intensity values. Scale bar: 50 μm. **F** Boxplots of normalised FN intensity of TCs under Blebb (left) and LPA (right) treatments. *n* = 33 (control), 39 (Blebb); 16 (control), 20 (LPA) follicles. **G** Box plot of number of pixels with intensity higher than threshold under different perturbations. *n* = 14 (control), 13 (Blebb); 10 (control), 10 (LPA) follicles. **H** Top: Schematic of perturbations on ovarian microtissues cultured ex vivo. Bottom: Representative images of nucleus (green) and fibronectin (magenta) labelled secondary follicle in an ovarian microtissue in control and Blebb conditions. Scale bar: 50 μm. **I** Zoomed-in images of actin (green) of the white boxes overlaid in (**C**). Scale bar: 10 μm. **J** Box plot of ratios of FN intensity in secondary follicles within microtissues under the different conditions. *n* = 10 (control), 14 (Blebb), 11 (LPA) follicles. Significance was determined by two-tailed Mann–Whitney U test (pairwise) in **B**, **F**, **G**, **J**. ns: $p > 0.05$. Boxplots show the mean (star), median (centre line), quartiles (box limits) and 1.5x interquartile range (whiskers). All data are from at least four biological replicates. Source data are provided as a Source Data file.

and Supplementary Fig. 6A). Since FN is not expressed in the primordial and primary follicle stages when the TCs are absent[39,40], we hypothesised that the TCs might be actively secreting the FN that eventually constitutes part of the matrix between the basal TCs and the BM. As the follicles mature, the variability of the matrix thickness increases (Supplementary Fig. 6B, C), suggesting active remodelling during development such as vascularisation during theca interna development[41,42].

Following a recent finding that contractile cancer-associated fibroblasts (CAFs) can produce fibronectin scaffolds around tumour cells for force transmission[17], we wondered if the TC contractility directly influences fibronectin assembly in ovarian follicles. In ex vivo follicles, we observed that blebbistatin treatment led to a significant reduction of normalised FN expression at the TC layer in the mid-section of follicles, while LPA treatment led to increased FN expression (Fig. 4E, top; Fig. 4F). The same trend was observed when we quantified the percentage of bright FN aggregates through 3D projections (Fig. 4E, bottom; Fig. 4G, and Supplementary Movie 3).

To confirm the in vivo relevance of our findings, we performed IF staining on ovarian microtissues to study how contractility perturbation impacts the FN expression in TC layers (Fig. 4H). We found that with Blebb treatment, the TCs surrounding the secondary follicles became rounder (Fig. 4I), similar to that observed in isolated follicles. Importantly, the FN intensity at the TC layers is significantly reduced in this condition (Fig. 4J), consistent with our findings in isolated follicles. Here, the observed swift FN remodelling in response to short-term pharmacological perturbations (4 hr) may be due to specific FN biosynthesis in early development that are distinct from the mature FN scaffold found in adult tissues[43].

We next investigated the role of FN in regulating compressive stress in follicles. By employing novobiocin, a small molecule inhibitor known to reduce extracellular fibronectin in cells[44,45], we found that reduced FN (Supplementary Fig. 5B, C) led to a significant decrease in pMLC expression (Supplementary Fig. 5B–D) in the TC layers. Novobiocin treated follicles also exhibit decreased follicle bulk modulus compared to the controls (Supplementary Fig. 5E), suggesting that reduced fibronectin expression renders the follicles more compressible. Together, this finding indicates the importance of TC-mediated fibronectin shell in maintaining compressive stress within the follicles.

Transient mechanical stress impacts GC YAP signalling and oocyte-GC communications

We next investigated if the signalling landscape within the follicles are sensitive to the mechanical environment. Inspired by previous studies showing that cell proliferation could be tuned by mechanical stress in cancer spheroids[16], we immuno-stained tissue slices and isolated follicles with Ki67, a known cell proliferation marker. We observed that the GCs in contact with the BM (basal GCs) were significantly less proliferative than the GCs surrounding the oocyte (oocyte GCs), both in situ and ex vivo (Fig. 5A, B). A similar pattern of differential proliferation between the basal- and oocyte GCs was also observed in follicles labelled with EdU (Supplementary Fig. 7A, B). We further immuno-stained the secondary follicles with YAP, a transcriptional co-activator known to be mechanosensitive[46] and is important for mammalian folliculogenesis[11]. We found that the YAP nuclear-to-cytoplasmic (N/C) ratio for basal GCs was significantly higher than that of the oocyte GCs (Fig. 5C, D), raising the intriguing possibility of a mechanical stress gradient within the follicle.

Next, we investigated if TC-mediated compressive stress could influence the YAP expressions of the oocyte- and basal GCs. We observed a significant increase in YAP nuclear translocation for follicles transiently treated (30 min) with LPA, Blebb and Y27632 (Fig. 5E–G). Prolonged treatment (2 h) of these drugs did not incur a significant change in EDU positive GCs (Supplementary Fig. 7A–C), suggesting that GC proliferation is not affected by perturbation of TC contractility at this timescale. Focusing on the transzonal projections, which are filopodia-like structures bridging the oocyte GCs to the oocyte that are essential for its growth[47], we found that the TZP number density reduced significantly upon Blebb and Y27632 treatment (Fig. 5H, I) but increased with LPA treatment. These treatments, however, did not impact the oocyte volume (Fig. 5J), suggesting that TC contractility can significantly impact GC-oocyte communications without oocyte volume retraction.

To exclude non-specific effects on GCs due to pharmacological treatments, we directly modulate compressive stress by physical means or targeting other follicular components that may regulate intrafollicular pressure, such as the BM. In *Drosophila*, collagenase has been reported to lower collagen IV contents in the BM[48], thereby lowering the BM stiffness and pressure in *Drosophila* ovarian follicles[49]. Using a similar approach, we found that disruption of the BM with minimal dosage of collagenase led to a decrease in the effective pressure (Fig. 6A). Though we observed only a minor increase in basal-GC YAP signalling upon short-term collagenase treatment (30 m), the impact on YAP nuclear translocation of both basal- and oocyte GCs was much more pronounced over longer timescales (2 h, Fig. 6B). However, the impact on GC proliferation was not significant (Supplementary Fig. 7B), similar to that by TC contractility perturbations. Interestingly, pMLC expression at the TCs reduced upon BM disruption (Fig. 6C), indicating further stress relaxation through TC-mediated mechanical stress. We next directly released the intrafollicular pressure by laser ablation at the BM, followed by post-fixation within minutes. Our results showed a striking increase in the YAP N/C ratios of GCs in laser ablated-follicles compared to the controls (Fig. 6D, E), similar to the effects by collagenase and contractility perturbations.

We next exert global compressive stress using dextran-based osmotic compression, which is known to increase tissue pressure in spheroids and organs[16,20]. Though it is not feasible to use AFM or laser ablation to directly probe the intrafollicular pressure of follicles placed in dextran medium, we did observe a significant reduction in the interstitial gap area in dextran-treated follicles (Fig. 6F), indicative of tighter GC packing and increased tissue pressure. Osmotic compression (10 kPa) led to increased YAP cytoplasmic localisation in both basal- and oocyte GCs (Fig. 6G), and reduced proliferation only in the oocyte-GCs (Supplementary Fig. 7B, C). Notably, the TZP number density reduced significantly upon osmotic compression and BM disruption (Fig. 6H), and the oocyte volume appeared more susceptible to osmotic compression than BM disruption (Fig. 6I). Altogether, our data provide strong evidence of compressive stress in regulating intrafollicular Hippo signalling pathway at short timescales (Fig. 6J), and that an appropriate amount of compressive stress is conducive to GC-oocyte bidirectional communications.

Major alterations of compressive stress lead to impaired follicle growth

To examine the functional consequence of compressive stress on follicle growth, we placed secondary follicles in control, Blebb and 10 kPa conditions and cultured them for four days (Supplementary Fig. 8A, B). By day 4, we observed a smaller follicle diameter in Blebb-treated and 10 kPa compressed follicles, compared to that of controls by day 4 (Supplementary Fig. 8C). Since it was difficult to grow these follicles in 2D beyond a certain size, we next cultured follicles by encapsulating them within 3D alginate hydrogels for similar number of days under the same conditions (Supplementary Fig. 9A, B). By day 3 post encapsulation, follicles treated with Blebb and 10 kPa showed smaller diameters than that of the controls (Fig. 7A, Supplementary Movie 4). As the follicle growth kinetics appeared to depend on the initial size, we sought to combine the growth kinetics of all follicles of arbitrary sizes into a master curve, thus allowing quantitative comparison of follicle growth in various conditions. By plotting the follicle growth rate per day versus size (Fig. 7B), we found that follicle growth is characterised by two phases: an initial pre-maturation phase where the growth rate increased linearly with its size, followed by the maturation phase ($D > 180\ \mu m$) where the growth rates reach a terminal value. While there was no difference between the three conditions at the pre-maturation phase, Blebb-treated and 10 kPa treated follicles showed significant growth attenuation at the maturation phase (Fig. 7C). Similar effects were also observed for follicles cultured in 2D

https://doi.org/10.1038/s41467-025-65390-y

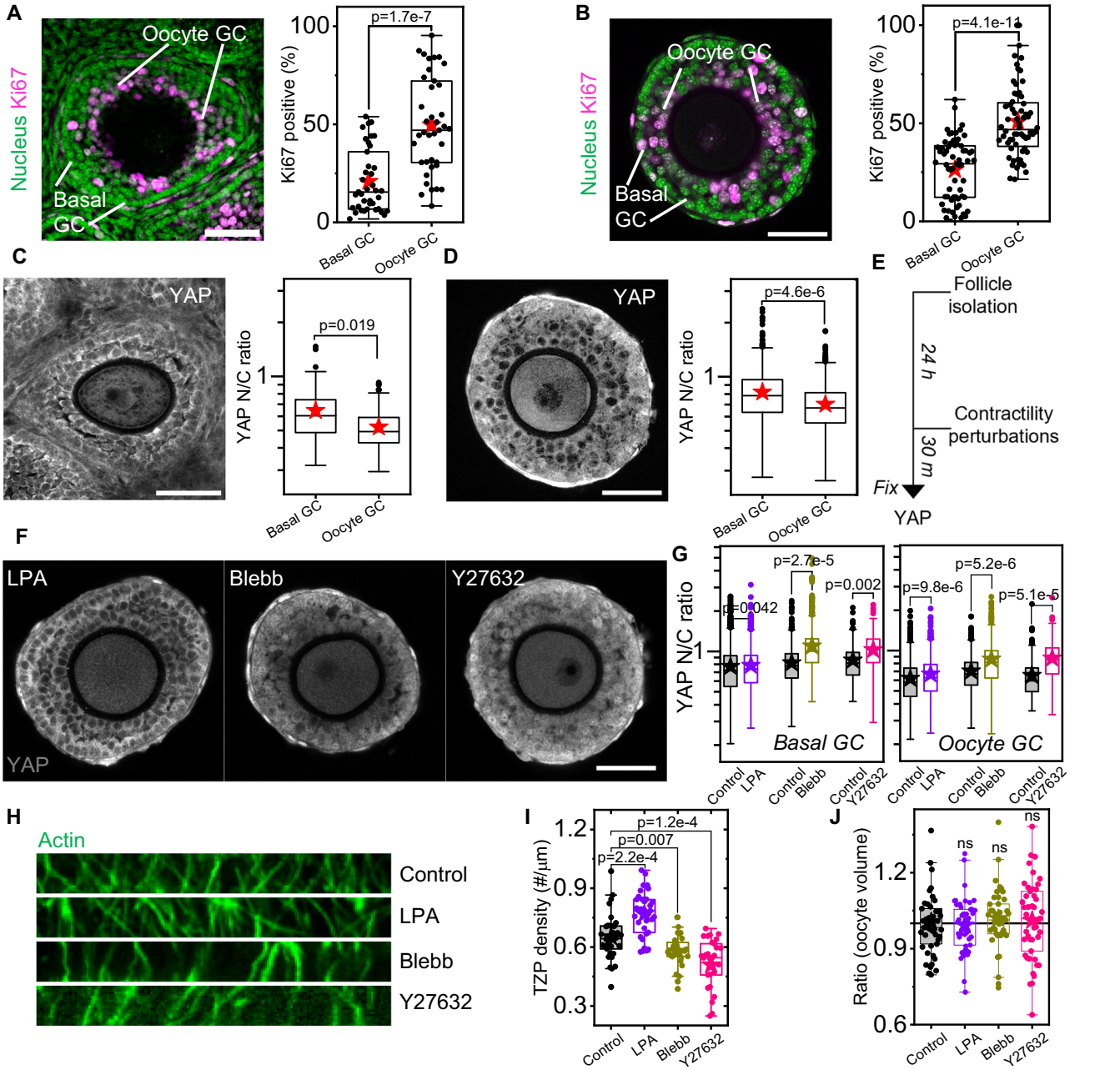

Fig. 5 | Transient perturbation of TC contractility impacts YAP signalling of granulosa cells and oocyte-GC communications. A Left: Representative image showing an ovarian slice labelled with DAPI (green) and immuno-stained with Ki67 (magenta). Scale bar: 50 μm. Right: Boxplots for percentage of Ki67$^+$ basal and oocyte GCs within secondary follicles in situ. n = 39 follicles. **B** Left: Representative image showing an isolated secondary follicle stained with DAPI (green) and Ki67 (magenta). Scale bar: 50 μm. Right: Boxplots for percentage of Ki67$^+$ basal and oocyte GCs ex vivo. $n = 67$ follicles. **C** Left: Representative image showing an ovarian slice immuno-stained with YAP in situ. Scale bar: 50 μm. Right: Boxplots of YAP N/C ratios (log scale) in basal and oocyte GCs in situ. $n = 12$ follicles. Scale bar: 50 μm. **D** Left: Representative image of the same follicle in (B) immuno-stained with YAP. Scale bar: 50 μm. Right: Boxplots of YAP N/C ratios (log scale) in basal and oocyte GCs ex vivo. $n = 67$ follicles. **E** Schematic showing how experiments were performed. **F** Representative images of follicles stained with DAPI and immunolabelled with YAP upon transient perturbation of mechanical stress. Scale bar: 50 μm. **G** Boxplots of YAP N/C ratios (log scale) in basal and oocyte GCs in various perturbations. $n = 38$ (control, LPA); 38 (control, Blebb); 19 (control), 30 (Y27632) follicles. **H** Representative images of actin transzonal projections between the oocyte and oocyte GCs for follicles in various perturbations, with corresponding Boxplots of TZP number density shown in (**I**). Scale bar: 10 μm. $n = 33$ (control), 34(LPA), 28 (Blebb), 29 (Y27632) follicles. **J** Boxplots of ratio (oocyte volume) under various mechanical perturbations. $n = 45$ (control), 46 (LPA), 41 (Blebb), 46 (Y27632) follicles. Significance was determined by one-sample t-test (t-test for mean=1) in (**J**) and two-tailed Mann–hitney U test (pairwise) in (**A**–**D**, **G**, **I**). ns: $p > 0.05$. Boxplots show the mean (star), median (centre line), quartiles (box limits) and 1.5x interquartile range (whiskers). All data are from at least four biological replicates. Source data are provided as a Source Data file.

(Supplementary Fig. 8D), providing further evidence that abnormal compressive stress impairs follicle growth.

To validate our findings in a more physiological context, we isolated ovary microtissues from the mice and cultured them under 10 kPa compressive stress (Supplementary Fig. 10A, B). We observed a linear increase in follicle growth rates, followed by a growth saturation above 180-200 μm (Supplementary Fig. 10C, left), similar to that observed for single follicles grown in 2D and 3D. The growth rate of

https://doi.org/10.1038/s41467-025-65390-y

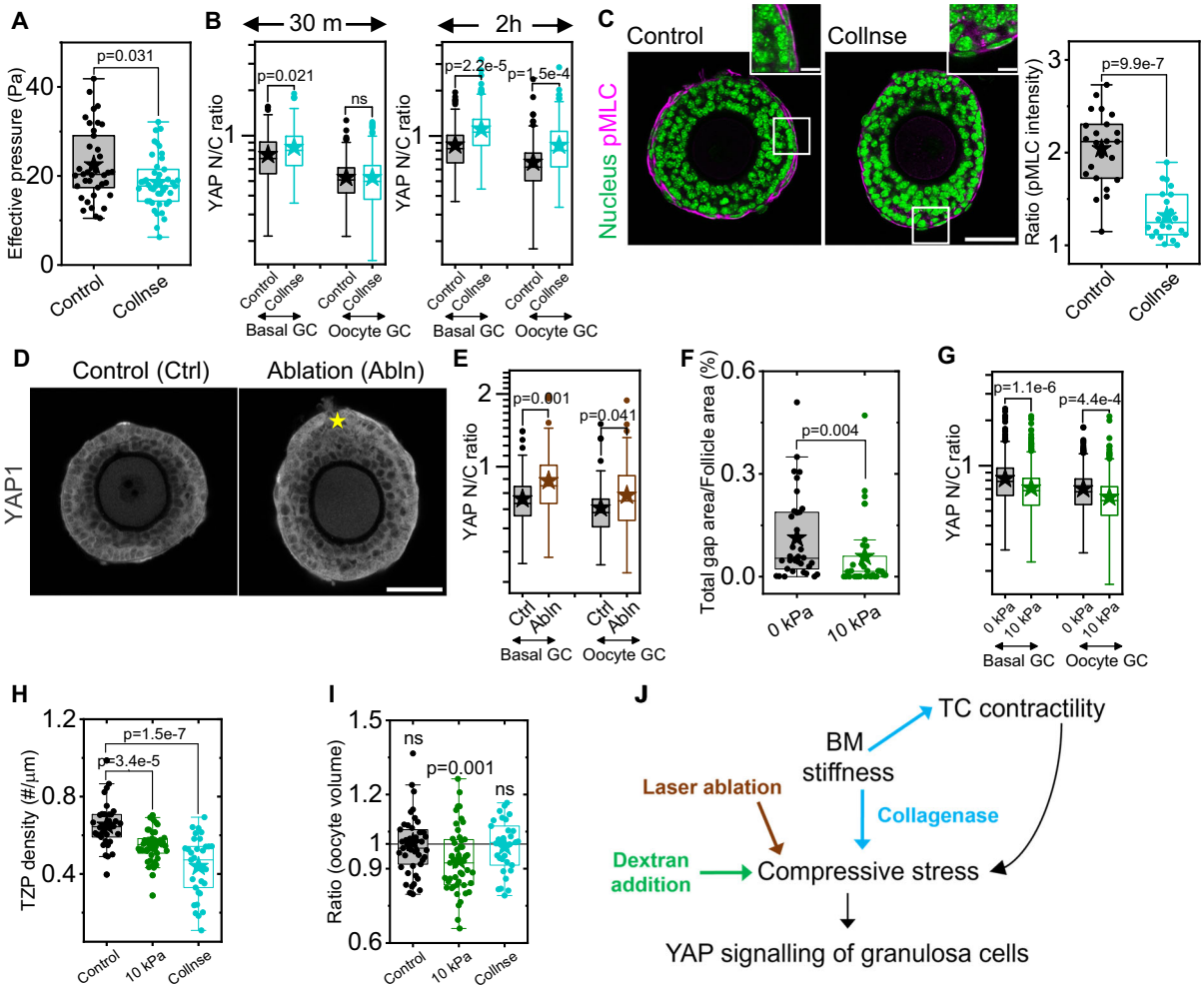

Fig. 6 | Physical perturbation of compressive stress affects YAP signalling of granulosa cells. A Boxplots for effective pressure measured by AFM in control and collagenase-treated (0.2 mg/ml, 30 mins) follicles. $n = 37$ (control), 42 (Collnse) follicles. **B** Boxplots of YAP N/C ratios of basal and oocyte GCs in control and collagenase-treated follicles (left: 0.2 mg/ml, 30 mins, right: 0.1 mg/ml, 2 hours). $n = 21$ (control), 24 (Collnse) follicles (left); $n = 21$ (control), 30 (Collnse) follicles (right). **C** Left: Representative images showing isolated secondary follicles stained with DAPI (green) and immunolabelled with pMLC (magenta) in different conditions. Scale bar: 50 μm. The inset shows a zoomed-in section of the images marked in white. Scale bar: 10 μm. Right: Boxplots for ratio (pMLC intensity) at TC shell in control and collagenase-treated follicles (0.2 mg/ml, 30 mins). $n = 23$ (control), 22 (Collnse) follicles. **D** Representative images of control and laser-ablated follicles immunolabelled with YAP (grey). A yellow asterisk marks the point of ablation. Scale bar: 50 μm. **E** Boxplots of YAP N/C ratio of basal and oocyte GCs in different conditions. $n = 18$ (control), 35 (ablation) follicles. **F** Boxplots of ratios of total interstitial gaps to follicle area for follicles under compression. $n = 34$ (0 kPa), 33 (10 kPa) follicles. **G** Boxplots of YAP N/C ratios (log scale) in basal and oocyte GCs under compression. $n = 47$ (0 kPa, 10 kPa) follicles. **H** Boxplots of TZP number density under different perturbations. $n = 33$ (control), 46 (10 kPa), 34 (Collnse) follicles. **I** Boxplots of ratio (oocyte volume) under various mechanical perturbations. $n = 45$ (control), 48 (10 kPa), 31 (Collnse) follicles in each condition. **J** Schematic representing how manipulation of compressive stress affects YAP signalling of granulosa cells. Briefly, changes in compressive stress by direct perturbations (either by using biophysical tools like laser ablation or by exogenously adding dextran), by perturbing basement membrane stiffness or by theca cell contractility affect the YAP signalling of granulosa cells. The colours in the schematic represent the colours used in the respective Boxplots. Significance was determined by one-sample t-test (t-test for mean=1) in (**I**) and two-tailed Mann-Whitney U test (pairwise) in **A**–**C**, **E**–**H**. ns: $p > 0.05$. Boxplots show the mean (star), median (centre line), quartiles (box limits) and 1.5x interquartile range (whiskers). All data are from at least four biological replicates. Source data are provided as a Source Data file.

dextran-treated follicles at the maturation phase was also significantly lower than that of the control (Supplementary Fig. 10C, right), with less oocyte extrusion events upon dextran treatment (Supplementary Fig. 10D and Supplementary Movie 5), again echoing our findings in 2D and 3D cultures.

To address the molecular mechanisms underlying decreased follicle growth in Blebb and 10 kPa conditions, we performed RNA sequencing, separately, on oocytes and GCs isolated from mature follicles grown in alginate gels for three days (Supplementary Fig. 9B). From the PCA plots, we found that the GCs cultured in different compressive stress conditions have distinct transcriptomic profiles (Supplementary Fig. 9C), which are also reflected in the heatmaps showing global differential expression patterns in these conditions (Supplementary Fig. 9D). Focusing on the volcano plots for Blebb vs. Ctrl, we found that reduced compressive stress led to downregulation of 74 genes and upregulation of 129 genes (Fig. 7D, left). Among the upregulated DEGs, many are involved in mechanotransduction pathways (e.g., *Piezo2*, *Icam1*). Others, such as collagen IVs (*Col4a1*, *Col4a2*, *Col4a3*), thrombospondin (*Thbs2*), Fibulin (*Fbln5*) and Fibrillin1 (*Fbn1*), are implicated in wound healing, tissue matrix remodelling and fibrosis. Other upregulated genes are linked to cytoskeleton regulation (*Acta2*, *Tpm1*, *Tpm2*, *Gsn*) and integrin signalling (*Itga5*), suggesting an active compensatory mechanism where cells attempt to restore mechanical homoeostasis by stiffening their own microenvironment. Interesting, many of the downregulated genes expressed are also implicated in mechanosignalling, such as those involved in ion channel

https://doi.org/10.1038/s41467-025-65390-y

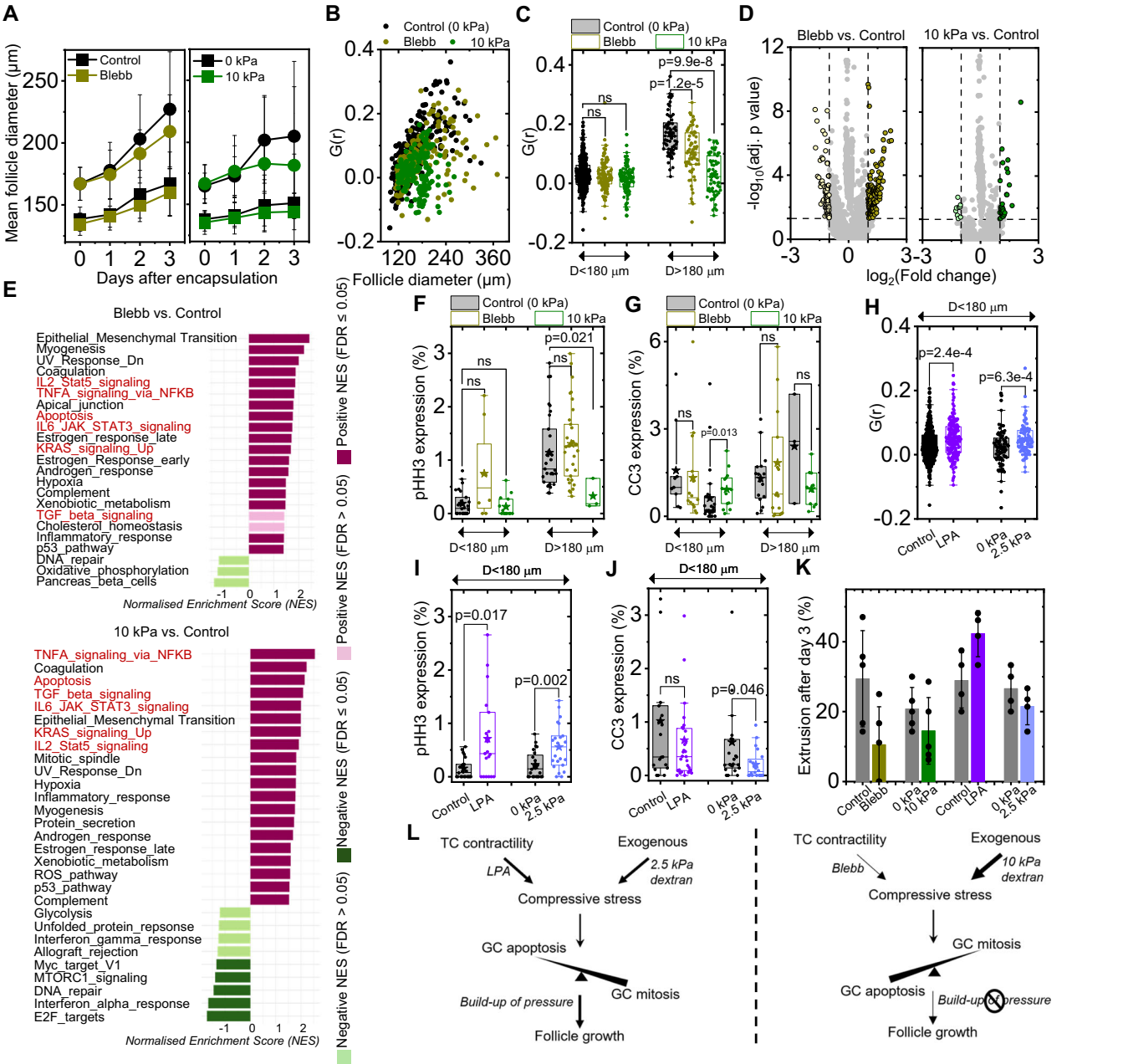

Fig. 7 | Attenuated or excessive compressive stress leads to reduced follicle growth. A Plot of mean follicle diameters (square: initial D < 150 μm, circle: initial D > 150 μm) in the different conditions. Data is presented as mean±SD. **B** Plot of growth rates per day vs. follicle size in different conditions. **C** Boxplots of growth rates at pre-maturation and maturation phases in different conditions. For **A**–**C**, $n = 96$ (control), 89 (Blebb); $n = 56$ (0 kPa), 61 (10 kPa) follicles. **D** Volcano plots of DEG analysis of RNA-sequencing of GCs in Blebb vs control and 10 kPa vs. control showing fold change (FC) expression. DEGs are identified when FC > 2 and $p < 0.05$(Wald test). $N = 4$ replicates for each condition. **E** GSEA shows normalised enrichment scores (NES, Benjamini-Hochberg test) for multiple hallmark gene sets in Blebb vs. control (top) and in 10 kPa vs. control (bottom). Same pathways similarly affected in both sets are in red. **F** Boxplots of pHH3$^+$ GCs in cultured follicles. $n = 57$ (control), 42 (Blebb), 17 (10 kPa) follicles. **G** Boxplots of CC3$^+$ GCs in cultured follicles. $n = 25$ (control), 32 (Blebb); $n = 28$ (0 kPa), 24 (10 kPa) follicles. **H** Boxplots of follicle growth rates in the pre-maturation phase in different conditions. $n = 72$ (control), 86 (LPA); 38 (0 kPa), 46 (2.5 kPa) follicles. **I** Boxplots of pHH3$^+$ GCs in cultured follicles at the pre-maturation phase. $n = 37$ (control), 40 (LPA) follicles; $n = 32$ (0 kPa), 32 (2.5 kPa) follicles. **J** Boxplots of CC3$^+$ GCs in cultured follicles at the pre-maturation phase. $n = 48$ (control), 55 (LPA) follicles; $n = 28$ (0 kPa), 29 (2.5 kPa) follicles. **K** Percentage of extrusion events upon compressive stress perturbations. Symbols represent the rupture events in each experiment; bars represent the mean, and error bars represent the standard deviation. N = 5 (Control/Blebb; 0 kPa/10 kPa); 4 (Control/LPA; 0 kPa/2.5 kPa). **L** Left: schematic showing minimal increase of compressive stress by LPA or addition of 2.5 kPa dextran (moderately thick arrows) enhances GC mitosis and reduces GC apoptosis while maintaining the intrafollicular pressure and promoting follicle growth. Right: schematic showing significant alterations to compressive stress (stress release by Blebb in thin arrow or stress increase by 10 kPa dextran in thick arrow) enhance GC apoptosis while reducing GC mitosis, leading to reduced intrafollicular pressure build-up and decreased follicle growth. Significance was determined by a two-tailed Mann–Whitney U test (pairwise) in **C**, **F**–**J**. ns: $p > 0.05$. Boxplots show the mean (star), median (centre line), quartiles (box limits) and 1.5x interquartile range (whiskers). All data are from at least four biological replicates. Source data are provided as a Source Data file.

regulation (*Trpm4* and *Slit1*) and cytoskeletal dynamics (*Dsp*, *Krt79*, *Pdlim4*, and *Dynlrb2*).

On comparing GCs cultured under higher compressive stress (10 kPa; Fig. 7D, right), we found that 9 genes were downregulated while 27 genes were upregulated. Of the 9 downregulated genes, Protein kinase C alpha (*Prkca*), Calcium/calmodulin-dependent protein kinase 1D (Camk1d), and PPFIA family member 3 (*Ppffia3*) are known to be linked to integrin mechanotransduction. ECM regulators (*Tgfbi* and *Mmp11*), stress responders (*Edn1*, *Rhob*, *Id1*, *Id2*, etc.) and cytoskeletal organisers (*Cdc42ep3*, *Fhdc1*) are among the upregulated genes in GCs cultured in enhanced compressive stress.

When comparing the top 50 clustered DEGs, we find that many genes were associated with mechanotransduction pathways (grey, Supplementary Fig. 9E). Among them is the gene encoding the tight junction Occludin (*Ocln*), which was upregulated under higher compression and downregulated during stress release. This suggests a dynamic remodelling of cell-cell junctions to alter tissue-level mechanics in response to distinct mechanical states. Gene set enrichment analysis (GSEA) further revealed that both compressive stress modulations upregulate hallmark genes of TNFα via NFκβ, Interleukin-6/JAK/STAT, KRAS, TGFβ signalling, which are all related to inflammation and integrin mechanotransduction responses (Fig. 7E). Other notable changes in both Bb and 10 kPa conditions were the upregulation of apoptotic hallmarks and downregulation of DNA repair in GCs (Fig. 7E), which were consistent with GSEA plots derived from KEGG (Supplementary Fig. 11A, B) and Reactome pathways (Supplementary Fig. 11C, D). We, also, note a distinct enrichment of the Hippo signalling pathway, only in 10 kPa condition (red asterisk, Supplementary Fig. 11B). Interestingly, when comparing the RNA sequencing results for oocytes, we observed no distinct clustering in PCA plots (Supplementary Fig. 12A) and no differentially expressed genes (Supplementary Fig. 12B) between the three conditions.

To confirm that the transcriptional changes leading to mis-regulated GC division in both Bb and 10 kPa conditions are reflected at the proteomics level, we stained post-cultured follicles for phospho-histone H3 (pHH3), a marker for mitosis, and cleaved caspase3 (CC3), an indicator for apoptosis (Supplementary Fig. 13A, B). We found that, in 2D cultures, the number of mitotic cells reduced, and the number of apoptotic cells increased on modulating compressive stress (Supplementary Fig. 8E, F). This effect was less pronounced in 3D cultures; where no significant difference was observed in GC proliferation and apoptosis between control and Blebb-treated samples (Fig. 7F–G, $D > 180\ \mu m$). With 10 kPa compression, we did observe a significant reduction in proliferation. Of note, there was no difference in the number of GCs at telophase between control and Blebb-treated follicles (Supplementary Fig. 13C), indicating that Blebb. treatment did not cause deleterious effects such as delayed cytokinesis.

Intriguingly, we observed that culturing follicles in conditions where compressive stress is minimally increased – either by increased TC contractility (LPA) or osmotic compression (2.5 kPa), promoted follicle growth at the pre-maturation phase (Fig. 7H, Supplementary Movie 6). This is consistent with these follicles having more mitotic cells (Fig. 7I) and lower number of apoptotic cells (Fig. 7J). We further observed that compared to the controls where typically ~20% of the follicles showed follicle rupture and oocyte extrusion in 3D culture (Fig. 7K), such events were greatly reduced in Blebb or 10 kPa conditions but increased with LPA treatment (~40%). This led us to hypothesise that optimal follicle growth could be a consequence of a buildup of intrafollicular pressure, regulated by a fine balance between GC proliferation and death. Minimal increase in compressive stress promotes cell division over apoptosis, leading to increased tissue pressure and follicle rupture as it counters the surrounding confinement pressure imposed by the gel (Fig. 7L, left). However, when the GC apoptosis exceeds mitosis, as are the case with abnormally high or low compressive stress, the intrafollicular pressure reduces, leading to reduced extrusion events (Fig. 7L, right). Overall, our data indicate that an optimal compressive stress is required for sustaining intrafollicular pressure and long-term follicle growth.

Discussion

In the past decades, significant progress has been made in understanding the roles of oocyte-granulosa cell signalling pathways[50], ECM and stroma[51] in ovarian biology. However, the origin and functions of theca cells that make up the periphery of preantral follicles remain poorly understood. While it has long been proposed that the theca externa may exert contractile forces to aid ovulation[52], existing studies on TCs remain largely limited to their steroidogenic functions[23,31], with little examination of their mechanical roles. This is highly pertinent given recent evidence that mechanical cues in the follicle microenvironment can regulate follicle activation, growth and ovulation[8,11]. Since direct measurement or manipulation of TC mechanics in ovaries is challenging, we developed a bottom-up approach to examine their mechanical functions ex vivo. By combining biophysical and pharmacological approaches, we revealed how TCs can generate compressive stress to regulate intrafollicular pressure, granulosa cell signalling and follicle growth.

We found that the TCs of murine secondary follicles are highly contractile, with surface tension significantly greater than that of highly stretched epithelial cells in living tissues[35], potentially due to their strong coupling to the underlying FN matrix. The contractile nature of TCs corroborates with recent optical elastography studies[21,53] showing that the TCs form a stiff shell around the follicles, potentially protecting the oocyte from excessive deformation. TCs appear to be fibroblast-like cells that can actively secrete FN in a contractility-dependent manner, which resembles contractile CAFs that are able to form a fibronectin-rich capsule around tumour cells and trigger mechanotransduction through compressive stress[17]. Inhibiting extracellular fibronectin expression negatively impacts TC contractility, hinting at potential feedback between TC mechanics and FN assembly. FN assembly has been shown to be mechanosensitive to tissue strain, such as during blastocoel expansion in early *Xenopus* development[54]. Whether follicle growth in turn generates tissue strain on TCs to trigger mechanosensing and FN assembly is unclear and constitutes an exciting topic for future research.

We demonstrate that transient abolishment of TC contractility leads to increased follicle size and decreased tissue elasticity, viscosity, and intrafollicular pressure, which is consistent with reduced follicle rupture events in 3D culture. The effect is less pronounced in the case of hyperactivation of TC contractility using LPA, suggesting that follicles in their native state are close to a maximally compact state that render them less susceptible to further compression. Indeed, we found that the secondary follicles are fairly non-compressible, with bulk modulus ~25 kPa. This translates to an apparent Young's modulus of 15 kPa, assuming the follicle's Poisson ratio to be close to 0.4, as reported for spheroids[55]. This value of Young's modulus is consistent with the observation that follicles in situ are often found to be deformed by the neighbouring follicles or stroma with comparable stiffness in the range of kPa[14].

The origin of the spatial patterns in GC YAP and Ki67 signalling is unclear. We propose that this could be regulated by mechanical or biochemical signalling from the BM or oocyte, or the presence of a mechanical stress gradient within the follicles that remains to be tested in the future. Pharmacological inhibition of TC contractility, laser ablation and BM degradation independently led to enhanced YAP nuclear transport of the GCs at short timescales. By contrast, global compression by dextran (10 kPa) leads to cytoplasmic YAP localisation and reduced proliferation of GCs, similar to what has been reported for cancer cell spheroids[56]. These data provide unequivocal evidence that GCs' YAP signalling respond rapidly to intrafollicular pressure, potentially due to mis-regulation of GC contacts[57,58] or contact

inhibition[59]. The striking decrease in TZP number density upon perturbation of TC contractility, BM integrity and 10 kPa compression revealed a strong coupling between intrafollicular pressure and functional oocyte-GC communications. The negligible impact of actomyosin perturbation or BM disassembly on oocyte size (Figs. 5J, 6I) suggests that the oocytes do not experience significant compression in their native state. However, they can be further compressed through dextran-induced global compression, implying dynamic fluid exchange between the oocyte and the surrounding GCs through gap junctions[60].

In this work, we uncover an initial size-dependent growth rate followed by a terminal growth rate at the maturation phase once the follicles grow past a critical size of 180 μm. Our finding is consistent with another report based on BrdU pulse-chase to track proliferating GCs and growth rates in vivo[61]. Such non-monotonous growth profile is in marked contrast to cancer spheroids which exhibit a constant growth rate independent of its size (logistic growth)[16]. On a functional level, our study revealed attenuated growth of follicles under drastic perturbation of compressive stress due to increased GC death and reduced proliferation (Fig. 7). Specifically, we showed that within the three-day culture period, the transcriptomic change within the follicles is primarily driven by the GCs affecting inflammatory responses, ECM remodelling, and integrin-mediated mechanotransduction, instead of a global change in the oocyte's gene expression program. Similar upregulation of ECM and inflammatory responses has been reported when follicles are subjected to a stiff environment in 3D[9], which also revealed mechanosensitive transcriptional changes at short timescales that gradually diminished at longer timescales. It remains an open question whether our observed transient impact on GC YAP signalling and TZP dynamics upon mechanical stress perturbation are linked to altered GC proliferation and apoptosis at long timescales. The lack of a significant change in cell proliferation and apoptotic markers with Blebb treatment in 3D, despite impaired follicle growth, suggests that other factors such as cell cycle length and tissue packing, may influence follicle growth. We cannot exclude possible off-target effects by Blebb and LPA on non-mechanical cellular processes such as signalling pathways or metabolism. Future work using genetic perturbations may elucidate the specific functions of TC mechanics during follicle development.

While we found that intermediate level of compressive stress promotes optimal follicle growth (Fig. 7L), our study does not determine the exact molecular mechanisms driving this behaviour. We propose that additional mechanisms such as osmotic regulation or improved gap junction dynamics in the GCs or the oocyte-GC interface might be implicated in this process. Future transcriptomics studies, combined with live imaging of intrafollicular dynamics and mechanical stress mapping using 3D force sensors[62], may reveal the interplay between mechanical stress and cell number control during folliculogenesis.

Our work adds to the growing list of evidence that compressive stress plays a central role in controlling various processes in development[19,20], diseases[17,63] and physiology[16]. Interestingly, we observed that the TCs from late secondary follicles in aged ovaries expressed reduced pMLC as compared to those from the young ones (Supplementary Fig. 14). Combined with recent work showing reduced GC proliferation and increased cell death in follicles during ageing[64], it is plausible that mis-regulated TC mechanics and intrafollicular pressure may contribute to impaired follicle growth during ovarian ageing[65]. Such dysfunctions may also be implicated in PCOS, where abnormal TC steroidogenic functions maybe linked to defects in TC mechanics. From a translational perspective, the mechanical insights highlighted in this study could inform assisted reproductive technology and improve in vitro maturation, paving the way for 'mechano-therapeutics' to address unmet clinical needs in infertility.

Methods

Animals

Mice were group housed in individually ventilated cages with access to water and food under a 12-h light/12-h dark cycle. Mouse rooms were maintained at 18–25 °C and 30-70% relative humidity. C57BL/6NTac female mice, aged P25 – P28, were euthanized by carbon dioxide asphyxiation followed by cervical dislocation. ICR female mice, aged 8 weeks and 14 months, was used for preliminary experiments reported in Supplementary Fig. 14. All animals were bought from Singapore InVivos. Ovaries were then dissected from the mice and transferred to an isolation buffer (IB) consisting of Leibovitz's L15 medium (Thermo Fisher, 21083027) supplemented with 3 mg/ml Bovine Serum Albumin (BSA, Sigma, A9647). All mice care and use were approved by the Institutional Animal Care and Use Committee (IACUC) at the National University of Singapore.

Pharmacological and dextran treatments

Blebbistatin (Selleck, S7099) was used at 20 μM and Y-27632 (Merck, Y0503) was used at 20 μM to inhibit cell contractility. LPA (Oleoyl-L-α-lysophosphatidic acid sodium salt, Sigma, L2760) was used at 20 μM to enhance cell contractility. 0.2 mg/mL collagenase was used to disrupt the BM at 30 min or in 0.1 mg/mL at 2 h. Novobiocin (N1628) were used at 500 μM for 6 h to perturb fibronectin. Transient perturbations were done for 30 mins; perturbations to check changes in pMLC/FN expression was done for 4 hours. Large dextran molecules (2 MDa, Sigma, D5376) were dissolved in growth medium in varying concentrations to generate 2.5 and 10 kPa osmotic pressures[66].

3D and 2D follicle culture

Follicles were mechanically isolated from dissected ovaries under the stereomicroscope attached to a thermal plate using tweezers in IB at 37 °C. Growth medium, consisting of MEM-α GlutaMAX (Thermo Fisher, 32561037) supplemented with 10% Foetal Bovine Serum (FBS, Thermo Fisher, 10082147), 1% Penicillin-Streptomycin (Thermo Fisher, 10378016), 1xInsulin-Transferrin-Selenium (Thermo Fisher, 41400045), and 50 mIU/ml follicle stimulating hormone (Sigma, F4021) was prepared. Individual follicles were transferred to each well in a 96-well non-treated plate and cultured in growth medium at 37 °C, 5% CO_2, 95% humidity overnight.

1% alginate (Sigma, 180947) was prepared in phosphate buffer saline (PBS, Gibco, 18912014) and mixed with growth medium in a 1:1 ratio. Follicles were mouth-pipetted to the 0.5% alginate solution, and hydrogels were formed by pipetting each follicle-alginate mix into the crosslinking medium for ~2 mins. The crosslinker consisted of 50 mM calcium chloride (Sigma, C1016) and 140 mM sodium chloride (1st BASE, BIO-1111). Once encapsulated, each gel was placed in 100 μL growth medium inside individual wells of Ultra-Low Attachment 96-well plate (Corning, CLS3474) and at 37 °C, 5% CO_2, 95% humidity for up to four days. For long-term cultures, half the volume of the growth medium was changed in each well every two days. The follicles were removed from the alginate hydrogels after four days using 10 IU/mL alginate lyase (Sigma, A1603) at 37 °C for 10-15 mins.

For culturing without encapsulation (referred to as 2D cultures), each follicle was placed in 100 μL growth medium inside individual wells of Ultra-Low Attachment 96-well plate and incubated at 37 °C, 5% CO_2, and 95% humidity for up to four days. Half of the volume of the growth medium was changed in each well every two days.

Low-input bulk RNA-seq

We identified encapsulated follicles in the different culture conditions that grew beyond 180 μm and removed the alginate from them. Immediately after retrieval, the follicles were mechanically separated into oocytes and granulosa cells (GCs) within 5–10 minutes. While 1-2 oocytes were pooled together, a few hundred GCs were pooled into

one sample set respectively. This was repeated individually for the different conditions to maintain similar levels of harvested RNA in each case. Each set of samples was promptly transferred into lysis buffer from the RNeasy Plus Micro Kit (Qiagen) and stored at −80 °C until RNA isolation. To minimise technical variability, RNA extraction was performed simultaneously for all biological replicates after the completion of all experiments. Total RNA was extracted using the RNeasy Plus Micro Kit (Qiagen), following the manufacturer's instructions, and eluted in RNase-free water before being stored at −80 °C.

The quality control of the extracted RNA for oocytes and granulosa cells was conducted using the TapeStation High Sensitivity RNA ScreenTape Analysis. The RNA integrity number (RINe) was checked, cDNA was synthesised by the NEBNext Single Cell/Low Input RNA Library Prep Kit for Illumina (NEB, E6420L). Sequence-ready libraries were prepared following the manufacturer's instructions. Each sample utilised 8 μL of total RNA for cDNA synthesis, with cDNA amplification performed over 15 PCR cycles. Libraries were indexed using the NEBNext Multiplex Oligos for Illumina (NEB, E6440L) and sent to NovogeneAIT Genomics (Singapore) for sequencing on the Illumina NovaSeq X Plus platform.

Ovarian microtissue culture

Ovarian microtissues, which are small chunks of the ovary consisting of 4 to 5 secondary follicles, were isolated from the mouse ovaries and placed in the desired media droplets (1.4 mL) on 0.4 μm polytetrafluoroethylene (PTFE) membrane cell culture inserts (Millicell, PICM03050) in six-well plates. The well plate was incubated at 37 °C, 5% CO_2 and 95% humidity for up to four days. Half of the media was changed every alternate day and the microtissues were imaged on the stereomicroscope every day. For timelapse imaging of the microtissues, the well plate was shifted to the IX83 microscope (Olympus) and imaged by a DP23M monochrome CMOS camera with a 4X objective for 48 h with 30 mins intervals in the same culture conditions.

Timelapse imaging of 3D cultures

A customised resin (Clear Resin V4) V-shaped well mould was 3D printed (Form 3, Formlabs) with the bottom diameter of 200 μm and the upper diameter of 2 mm. To fabricate the microwells, PDMS mixture (10:1) was transferred onto the resin mould, peeled, and then glass-bonded to a 2-well chamber slide using a plasma cleaner. The chamber slides housing the microwells were sterilised before follicle encapsulation.

Alginate solution (4 μL) was first added to each well. Desired follicles were placed in the alginate, one in each well, and then topped in the crosslinker solution (3 μL). After 2 mins, 2 mL of required growth medium was added to each chamber and taken to the microscope (IX83, Olympus). Images were captured by a CMOS monochrome camera (DP23M) with a UPLXAPO10X objective for 60 hours with 30 mins interval at 37 °C, 5% CO_2 and 95% humidity.

Bead-follicle assays

Follicles were placed in the follicle medium filled with EGFP-CNA35 membrane dye (Cellbrite, 30083) for 1-2 hours to distinguish the BM and the outer theca cells. They were then washed thrice before being transferred to 200-μl droplets of follicle medium filled with the gelatin beads (kind gifts from Krystyn van Vliet's lab) in a 35 mm glass-bottom dish (Cellvis, D35-10-1.5-N) covered with mineral oil (Sigma, M8410). The beads and follicles are manipulated to position them in contact and cultured in an incubator with a humidified atmosphere supplemented with 5% CO_2 at 37 °C for up to 2 hours. Time-lapse imaging for bead-follicle fusion was performed on a Zeiss LSM 710 confocal microscope with an onstage incubator using 40×/NA 1.2 W Corr objective and Zen 2012 LSM software with 488 nm and 633 nm lasers. Image stacks were acquired at 90 mins intervals with 4 μm z-steps. For bead-follicle experiments performed in the presence of blebbistatin, the follicle medium (volume increased to 400 μl) was not covered with mineral oil.

Tissue sectioning

Ovaries were fixed in 4% paraformaldehyde (PFA, Santa Cruz Biotechnology, sc-281692) at room temperature (RT) for an hour. The fixed ovaries were washed in washing buffer (WB, 1% BSA in 1X PBS) thrice before being embedded into 4% low-melting point agarose (Thermo Fisher, 16520100). The embedded tissue was sliced into 100 μm thick tissue sections using a vibratome (Leica Microsystems, VT1200S) in PBS at 0.05 mm/s speed and 1 mm amplitude.

Immunofluorescence (IF) staining

Isolated follicles were fixed in 4% PFA at RT for 30 mins and washed with WB thrice before immuno-staining. Fixed follicles and tissue slices were incubated in blocking-permeabilizing solution (3% BSA and 0.03% Triton X-100 (Sigma, X100)) at RT for 2–4 h, followed by incubation at 4 °C in primary antibodies diluted in the blocking solution overnight. The tissues were washed 5 times in WB and incubated in secondary antibodies diluted in the washing buffer for 4 h at RT. They were washed thrice in WB before mounting. The ovarian slices were mounted into ProLong Gold antifade mountant (Thermo Fisher, P10144) and left to cure overnight at RT, whereas isolated follicles were mounted into SlowFade Gold antifade mountant (Thermo Fisher, S36940) prior to imaging.

Primary antibodies used were rabbit anti-phospho myosin light chain 2 (Ser19) (Cell Signalling Technology, 3671 L, 1:100), rabbit anti-fibronectin (Abcam, ab2413, 1:100), rabbit anti-Ki67 (Cell Signalling Technology, 9129S, 1:100), rabbit anti-phospho histone H3 (Cell Signalling Technology, 9713 T, 1:100), rabbit anti-cleaved caspase 3 (Abcam, ab2302, 1:100), rabbit anti-VCAM1 (Cell Signalling Technology, 39036S, 1:100), rabbit anti-NR2F2 (Abcam, ab211777, 1:100), rabbit anti-CYP11A1 (Cell Signalling Technology, 14217, 1:100), rabbit anti-CYP17A1 (Cell Signalling Technology, 94004 T, 1:100), rabbit anti-YAP (Cell Signalling Technology, 14074S, 1:100, for tissue slice) and mouse anti-YAP (Abnova, H00010413-M01, 1:100, for isolated follicles). Alexa Fluor 488 labelled anti-mouse (Invitrogen, A32766, 1:500) and Alexa Fluor 546 labelled anti-rabbit (Invitrogen, A10040, 1:500) was used as secondary antibodies. DNA was stained with DAPI (Sigma, D9542, 2 μg/mL) and F-actin was stained with either Alexa Flour 488-labelled phalloidin (Invitrogen, A12379, 1:1000) or Alexa Flour 633-labelled phalloidin (Invitrogen, A22284, 1:300).

All fixed samples were imaged with a Nikon A1Rsi confocal microscope with NIS Elements. Isolated follicles were imaged using Apo 40×/1.25 WI λS DIC N2 objective at 4 μm z-slices. Tissue slices were imaged with Plan Apo VC 20×/0.75 DIC N2 and stitched with 10% overlap using lasers 405 nm, 488 nm, 561 nm and 640 nm.

For microtissue IF (Fig. 4H), microtissues were isolated and placed in media droplets on membrane inserts as described in a previous section for a day. The inserts are then transferred to the desired solutions (control, Blebb (20 μM), and LPA (20 μM)) for 4 hours. The microtissues are then fixed on the inserts with 4% PFA and immunostained in the same procedure as described above.

EdU incorporation assay

Follicles were incubated with 10 μM EdU (EdU Staining Proliferation Kit, abcam, ab219801) for 30 min under optimal growth conditions. They were washed with WB and were fixed and permeabilized. The EdU reaction solution was prepared as per the manufacturer's specifications. The follicles were incubated in the reaction solution for 2 h at RT in the dark. They were washed and incubated with DAPI for 2 h at RT in the dark before being washed and then mounted for imaging.

Atomic force microscopy

Sample preparation and setup for single cell and follicle indentation. Wafer for the PDMS microwells was designed by the lab. PDMS and cross linker were mixed in 10:1 ratio and degassed before transferring to the wafer. The PDMS mixture was degassed again and cured at 80°C for two hours. The PDMS mould was removed and trimmed into working size. To fabricate the microwells, PDMS mixture was transferred onto the glass bottom dish (WPI FD35) and the trimmed PDMS mould was placed inverted on top and cured at 80 °C for two hours. The mould was then removed and the PDMS microwells were used for AFM. The microwells were filled with growth medium and left in the 37 °C incubator for at least 30 mins. Freshly isolated follicles were transferred to medium and left to stabilize under optimal growth conditions before being indented.

The NanoWizard 4 BioScience (JPK Instruments AG) mounted on an inverted microscope (Olympus IX81) with a 10x objective was used. Polydimethylsiloxane (PDMS) microwells with 100 μm, 130 μm, 150 μm diameters at 50 μm spacing and 80 μm depth were fabricated to house the follicles during AFM experiments.

A pyramidal tip on Bruker MLCT-D cantilever (0.03 N/m spring constant) was used to measure effective TC surface tension. A polystyrene particle (45 μm) on silicon nitride cantilever (Novascan Technologies, PT.PS.SN.45, 0.35 N/m spring constant) was used to measure bulk tissue mechanics. Measurements were conducted with a constant speed of 5 μm/s, with a loading force of 10 nN (tip) or 15 nN (bead) in a 10 μm by 10 μm area. Both sensitivity and spring constant were calibrated using a contact-based approach prior to each experiment. Follicle diameters and effective tip radius were determined from the brightfield images.

Primary cell isolation. Primary theca and granulosa cells were isolated based on protocols adapted from Tingen et al.[36]. In brief, freshly isolated ovaries were poked in IB by a needle under the stereomicroscope to release the GCs till intact follicles were no longer observed. This solution was centrifuged at 94 × *g* for 5 min. The pellet was washed twice and resuspended in McCoy's 5 A medium (Gibco, 16600082) supplemented with 5% FBS and 1% Penicillin-Streptomycin to yield primary GCs.

A digestion buffer comprising 0.05 mg/mL activated DNase I (DNase I with HBSS in a 1:1 ratio, Merck, 11284932001), 10 mg/mL Collagenase (Thermo Fisher, 17104-019), and 40% Medium 199 (Gibco, 11150067) was freshly made. The remaining tissue fragment after mechanical disruption containing theca cells (and stromal cells) was washed and transferred to the digestion buffer (200 μL per ovary). This was incubated at 37 °C for 1 h, mixing gently every 15 min using a pipette. Once completely dissolved, the solution was centrifuged at 94 g for 5 min. The pellet was washed and resuspended in supplemented McCoy's medium. Cells were then seeded onto 6-well plates in the growth medium and incubated at 37 °C, 5% CO_2 and 95% humidity for at least a day before further experiments.

Traction force microscopy (TFM)

Preparation of TFM substrates. The protocol was adapted from Huang et al.[67]. In brief, glass coverslips were cleaned with 2% Hellmanex III (Sigma, Z805939), washed with water, and blow dried with nitrogen before silanization. They were incubated in the silanization solution, 2% trimethoxysilyl propyl methacrylate (TMPMA, Sigma, 440159) and 1% glacial acetic acid in absolute ethanol for 10 min, rinsed with ethanol, blow dried with nitrogen, and incubated at 120 °C for an hour.

An aliquot of 3 μl of 100 nm fluorescent microspheres (F8810, Invitrogen) was added to 10 ml of milliQ water and sonicated for 10 mins. The bead solution was filtered by a 0.22 μm syringe filter (Sartorius) into 500 μL of 500 mM MES buffer (pH 6.0). A master polyacrylamide solution was made by mixing 200 μL of 40% polyacrylamide solution (Biorad, 1610140), 200 μL of 2% bis-acrylamide solution (Biorad, 1610142), 1.5 μL TEMED (Sigma, 411019), and 582.5 μL of the bead solution. A total of 16 μL of 10% ammonium persulphate (Biorad, 1610700) was added to the master mix, and 100 μL droplets were dispensed on a clean parafilm strip. The silanized coverslips were gently placed on the gel droplets such that the gel covered the whole glass area, and the polyacrylamide was allowed to gel for 30 mins. The coverslips with the gel were removed from the parafilm by floating water at the bottom of the gel and placed gel side facing upwards in PBS at 4 °C overnight after washing with 1X PBS thrice.

The gel was soaked in 0.1 M HEPES (1st BASE, BIO-1825, pH 7.4) for 30 mins. A 0.02 mg/mL solution of sulfosuccinimidyl 6-(4'-azido-2'-nitrophenylamino) hexanoate (sulfo-SANPAH, 803332, Sigma) was prepared in anhydrous DMSO. 1 μL of this sulfo-SANPAH solution was added to 20 μL of 0.1 M HEPES (pH 7.4). This solution was added to the polyacrylamide gel surface after discarding the HEPES that was soaking the gel. Mechanical agitation by a silicone block was done to ensure that sulfo-SANPAH was distributed uniformly. The gels were UV-treated in the UV-KB9 (KLOE, France) at 8% power for 5 minutes, and washed twice in 0.1M HEPES (pH 7.4). The process was repeated with a fresh solution of sulfo-SANPAH. The gels were washed twice with 0.1 M HEPES (pH 7.4) and once with 1X PBS.

A 100 μg/mL solution of collagen I (Sigma, C4243) was prepared in 1 X PBS. 250 μL of this solution was added to the gel and incubated in the dark for 2 hours at room temperature with intermittent mixing with a pipette to avoid clumping. The gels were washed thrice with 1 X PBS and stored in PBS before seeding of cells.

TFM setup. A spinning disk-confocal microscope with a Yokogawa CSU-W1 scanner unit (Yokogawa Electric, Japan), an iLAS laser launcher (Gataca Systems, France), and a sCMOS Camera (Prime 95B 22 mm, Teledyne Photometrics, USA) attached to a Nikon Ti2-E was used. Images were acquired by a 40x water immersion objective (CFI Apo LWD 40XWI λS N.A. 1.15, Nikon) at z-steps of 0.275 μm with the help of MetaMorph advanced acquisition software (Molecular Devices, USA). Coverslips with the polyacrylamide gels were placed in stainless steel cell culture vessels and 500 μL of supplemented McCoy's cell culture medium was added. Custom-made lids were used to control temperature, CO_2, and humidity while imaging. A z-stack of the fluorescent labelled beads was captured when the cells were adhered to the gel. 1% sodium dodecyl sulphate was prepared in the supplemented culture medium and 100 μL of this was added to the gel. A second z-stack of the beads was acquired with the same settings after 30 mins.

Scanning electron microscopy (SEM)

Ovaries were fixed with 2% PFA and 3% glutaraldehyde (GA, Ted Pella, 18427) overnight at 4 °C. They were washed thrice with PBS for 5 mins each. Samples were incubated in 1% osmium tetraoxide (OsO4, Electron Microscopy Systems, 19110) with 1.5% potassium ferrocyanide in PBS for 1 hour on ice and then washed thrice with distilled water for 5 min each. The samples were then placed into 1% thiocarbohydrazide (TCh, Electron Microscopy Systems, 21900) in distilled water for 20 mins at room temperature and washed thrice with distilled water for 5 mins each. The samples were then placed into 1% OsO4 in distilled water for 30 min at room temperature and washed thrice with distilled water for 5 min each. They were next incubated with 1% uranyl acetate (UA, Electron Microscopy Systems, 22400) in distilled water overnight at 4 °C and washed thrice with distilled water for 5 min each. 0.02 M lead nitrate (Electron Microscopy Systems, 17900) and 0.03 M aspartic acid (Merck, 100126) were mixed, and pH was adjusted to 5.5. The samples were kept in lead aspartate solution for 30 min at 60 °C in the oven and again washed thrice with distilled water for 5 min each. Tissues were dehydrated with ethanol (Fisher Scientific, 12498740), increasing gradually from 25%, 50%, 75%, 95% and 100%, with 10 min in

each solution on ice before washing with acetone (Fisher Scientific, 10252232) twice for 10 min each on ice. For resin infiltration, the samples were placed in 1:1 acetone-araldite resin mixture (Electron Microscopy Systems, 13900) for 30 mins and then 1:6 mixture overnight. They were then transferred to pure araldite for 1 hour in a 45 °C oven. This was done thrice before they were transferred into embedding mould with pure araldite and cured for 24 hours in a 60 °C oven.

The embedded samples were then sectioned using a Diatome diamond knife (Electron Microscopy Sciences, 27-ULDa) with the Leica UC6 ultramicrotome, and 100nm ultrathin sections were collected onto silicon wafers. SEM Imaging was done with Thermofisher FEI Quanta 650 FEG-SEM where large area montage scans were acquired with MAPS 2.1 software using the backscatter mode (vCD detector) at 5 kV, 5 mm working distance (WD).

Laser ablation

Follicles were stained with EGFP-CNA35 at 8 μM for 2 hours in follicle growth medium to label the BM. Laser ablation experiment was performed on a NikonA1R Multiphoton laser scanning confocal microscope with an Apo 40x/ NA 1.25 WI λ S DIC N2 objective lens. UV laser with 355 nm, 300 ps pulse duration and 1 kHz repetition rate (PowerChip PNV-0150-100, team photonics) was irradiated to the BM in the follicle equatorial plane for 5 secs at 300 nW laser power at the back aperture. For YAP experiments, the follicles were fixed within 2–5 mins after ablation. For velocity calculation, transmitted light (TD) and EGFP channel images were obtained every 2 secs for 10 mins.

Micropipette aspiration

Glass capillaries (World Precision Instruments, TW-100-3) were pulled using a pipette puller (P-97, Sutter Instrument) using a setting of ramp +3-5, pull 50, velocity 50, time 50, and pressure 500. The needles were cut to form 20 ± 3 μm (for single TC measurements) and 27 ± 2 μm (for TC shell surface tension) using a microforge (Narishige MF2). The micropipette was mounted on a micromanipulator (Narishige, MMO-4) and connected to a PBS-filled reservoir. The reservoir was connected to a microfluidic pump (Fluigent, Flow EZ) attached to a vacuum pump and the height of the reservoir was controlled by a translating stage (Newport). The micropipette was made to contact the TC surface, and pressure was increased stepwise with a 10 Pa increment using the Oxygen software (Fluigent) till a deformation of the micropipette radius (R_p) was achieved.

Quantification and statistical analysis

Quantification of basal TC-BM matrix thickness. Line-scans (~1.5 μm) were drawn perpendicular to the matrix between the basal TCs and BM in the SEM images, spaced 20 μm away from each other. Plot profiles were plotted; and the x-coordinates of the start and end of the "bright" matrix was noted from each intensity profile. The width of each profile was calculated by subtracting the x-values and averaged over all widths obtained from all line-scans in a follicle.

Quantification of pMLC and FN expression. Using FIJI, the z-plane where the oocyte diameter was the largest in the entire image stack was selected. A polygonal selection tool on the phalloidin-stained actin channel was used to mark the TC layer and the GC layers in follicles. The selection was overlaid on the pMLC/FN channel, and the mean intensity of the selection was measured. A 60 ×60 pixels area was demarcated in the same z-plane in the background of the image using the rectangle selection tool and the mean intensity of this area was measured. The ratio of the mean intensity of the signal to that of the background was termed as pMLC or FN expression. The ratio of the TC to GC mean intensity was termed as ratio (pMLC or FN intensity). Follicles of similar size imaged with the same z-plane and acquisition settings were used to quantify the number of pixels in the entire follicle volume having fibronectin intensity greater than a threshold. The threshold was set at 70% of the maximum intensity across the entire volume acquired on that day.

A segmented line tool was used to mark the oocyte cortex. The selection was overlaid on the pMLC channel, and the mean intensity was measured. By dividing this value by the mean intensity of the background, the ratio (pMLC intensity) at the oocyte cortex was computed.

Quantification of RNA sequencing data. Raw FASTQ files were processed using the nf-core/rnaseq pipeline, a standardised and reproducible bioinformatics workflow built using Nextflow[68]. The resulting gene count matrix was imported into R (version 4.5.1) for downstream analysis. Differential gene expression (DEG) analysis was conducted using the DESeq2 package[69]. Genes with an absolute log2 fold change ≥ 1 and an adjusted p-value < 0.05 were considered significantly differentially expressed. For pathway analysis, Gene Set Enrichment Analysis (GSEA) was performed using gene sets for Mus musculus from the MSigDB Hallmark collection, KEGG pathways, and the Reactome pathways.

Quantification of AFM-based indentation. The details of AFM-based analyses are explained in Supplementary Information.

Analysis of effective TC surface tension and effective follicle pressure. There is a linear regime of force-displacement relationship for indentation depth within 100-700 nm. The linear coefficient, here, is related to the hydrostatic pressure exerting at this shell[70,71] (details in Supplementary Material Sec. 1.a). Assuming a material homogeneity at the scale of follicle size, this pressure could be regarded as an effective hydrostatic pressure of follicle, and its surface tension (mostly contributed by theca cells) was then inferred from Laplace law as

$$\sigma_\infty = \mathrm{PR_f}/2, \tag{1}$$

where R_f is the follicle radius.

Analysis of tissue elasticity and hysteresis. For indentation depth within 1-5 μm, which is much smaller than the size of the probing bead and follicle radius, we used a Maxwellian viscoelasticity model to extract the pure elastic parts of the approach and retraction curves. The pure elastic force-indentation curve was then fitted by a simple Hertz model for a bead tip. Hysteresis was calculated as the area under the curve between approach and retraction plots.

Quantification of local parallel velocity. PIV analyses were implemented onto the time-lapse images obtained after laser ablation using openPIV in Python. The range of local area around the ablation point was determined by the GC layer thickness. The velocity of GC cells flowing away from the follicle centre was quantified as the mean velocity in this local range projected along the direction pointing from ablation point to the follicle centre.

Quantification of follicle and TC surface tension. Circles were fitted to find the radius of the aspiration volume (R_{asp}) in the micropipette and the radius of the local surface of the follicle or cell (R_c) being aspirated. The follicle or TC surface tension was calculated at steady state by the Young-Laplace's law as:

$$T = \frac{\Delta P}{2\left(\frac{1}{R_{asp}} - \frac{1}{R_c}\right)} \tag{2}$$

where ΔP was the pressure used to deform the follicle or cell respectively.

Quantification of bulk moduli for follicles and beads. A polygonal selection was drawn on the edge of the follicle/bead using FIJI. The Fit Ellipse option was used to measure the major (a) and minor (b) axes of the selection. Volume of the selection was calculated by

$$V = \frac{4}{3}\pi\frac{ab^2}{8}. \quad (3)$$

The difference (ΔV) between the initial and final volume was computed for every osmotic pressure and the ratio of the difference to the initial volume at each osmotic pressure was plotted with the corresponding osmotic pressure:

$$\Delta P = K\frac{\Delta V}{V}, \quad (4)$$

where K is the bulk modulus. Negative data points were removed, and the average curve was generated. The linear part of the average plot, between 0 and 5 kPa (Fig. 2, Supplementary Fig. 4) and between 0 and 2.5 kPa (Supplementary Fig. 5), was fitted to a straight line with the intercept fixed at 0 and the slope was measured. All slopes with goodness of fit (R-square) > 0.75 was considered, the inverse of the slope was calculated and termed as bulk modulus.

Quantification of TC compressive stress. The z-plane of the image stack (captured at t = 0 hr) with the maximum bead diameter was determined. A maximum intensity projection was obtained from 5 slices (the max. bead diameter z-plane, 2 slices before and 2 slices after that). The outline of the bead was demarcated, and the volume of the bead is measured. The same was done for the image stack at t = 40 h, and the change in volume between these two timepoints was calculated. The compressive stress was then computed by multiplying the relative volumetric change of the beads to its bulk modulus.

Quantification of TC and GC ALP staining, circularity and traction stress. A polygonal selection was drawn on each cell boundary using FIJI. Circularity of individual cell was measured by the Shape descriptors option. Mean intensity of the same selection was also measured. The mean intensity of a 10 × 10 pixels area in a non-cell area (background) was also measured. Normalised ALP stain was calculated by dividing the mean intensity of the background by that of individual cells.

Images of the same cells with and without beads (after SDS washing) were stacked to create an image pair using FIJI. An ImageJ plugin, Align Slice, was used to align for any drift away from the cell boundary. The cell boundary was noted from the corresponding brightfield image. The bead displacement field and magnitude were calculated using the PIV plugin using the same iteration scheme (128/256 for 1st pass, 64/128 for 2nd pass, and 32/64 for 3rd pass). The threshold, or the cross-correlation coefficient, was set at 0.60. The traction stress field and magnitude were computed by the FTTC plugin using 32 kPa as the stiffness, 0.5 as the Poisson ratio, and 9×10^{-11} as the regularisation factor. The stress fields were read out as images in FIJI; the cell brightfield images were used to outline the boundary of the cells, and stress clusters within each cell were identified by overlaying the cell ROI using the Particle Analysis plugin. The cluster ROIs were then overlaid on the stress magnitude images; average and maximum stress from each cluster was then measured.

Quantification of follicle and oocyte volume upon transient perturbations. Freshly isolated follicles (one in each well) were placed in growth medium, and images of each follicle were immediately captured. They were incubated at 37 °C for 30 mins and images of each were acquired again. They were then transferred to a medium containing perturbations, and images were captured. The follicles were imaged again after 30 min and transferred to normal growth medium. Images were taken instantly and then after incubating for 30 min at 37 °C. Each follicle, thus, could be tracked over six images. Follicle volume was calculated as mentioned in the previous section. The ratio between follicle volume at t = 30 h and t = 0 h for each condition (control, treatment, recovery) was termed as ratio (follicle volume).

A polygonal selection was drawn around the edge of zona pellucida using FIJI. The major (a) and minor (b) axes of the selection was measured by the Fit Ellipse option. Volume of the selection was calculated by Eq. (3). The ratio between oocyte volume at t = 30 hr and t = 0 hr for each condition was termed as ratio (oocyte volume).

Quantification of GC proliferation and YAP signalling. The z-plane of the image stack (isolated follicles and tissue slices) with the maximum oocyte diameter was determined in FIJI. The number of DAPI-stained nuclei and Ki67-labelled nuclei in this layer was counted separately. The ratio between the Ki67 + /DAPI+ was calculated, and the value was termed Ki67 positive. The same approach was taken for the EdU proliferation analysis.

Nuclei and cytoplasm of each GC were identified using the DAPI and DAPI/Phalloidin overlay, respectively. A 2 × 2 pixel selection was drawn on each of the nucleus and its corresponding cytoplasm. These selections were overlaid on the YAP channel, and the mean intensity was measured for each selection. The ratio of the nuclear to cytoplasmic selections for each cell was calculated and plotted.

Quantification of number of Transzonal projections (TZP). The z-plane of the image stack with the maximum oocyte diameter was determined. The intensity of the background of the sample was measured at this plane. A segmented line was drawn on the zona pellucida surrounding the oocyte using the Line ROI tool in FIJI. The length of this line was measured. The intensity of the actin-labelled image was plotted as a function of the length of the line using Plot Profile in FIJI. The data was used to count the number of peaks above the background value using Origin2021b. The ratio of the number of peaks to the length of the line was termed as number density.

Quantification of interstitial gap within follicles. A pixel was detected as interstitial if its intensity was below the background noise level in all three channels of DAPI, Actin and YAP. A cluster of connected interstitial pixels was recognised as one interstitial gap. Each cluster has an area of A and perimeter length of P, the shape of each cluster is quantified as the ratio, which is 1 for a sphere and larger than one for an elongated shape. All algorithms were developed with OpenCV in python.

Quantification of pHH3 and CC3-positive GCs. A mask was created to remove TCs from the images during quantification. Half of every follicle, ranging from the bottom-most z-plane to the equatorial plane, with the clearest signal was considered for analysis to avoid improper counting. Cell nuclei segmentation was performed on the DAPI channel using a Birch clustering algorithm. Pixels close to one cluster seed was identified as one cell. Image processing codes were implemented by Python. Birch algorithm was implemented through the scikit-learn module. A heurist parameter-tuning method was applied to the algorithm without assigning a cluster number to search for the optimal cluster (cell) size that would minimises the within-cluster-sum (wss) score. Then, the algorithm was looped over a reasonable range of cluster numbers, using this optimal cluster size to find the optimal cluster (cell) number that had the lowest WSS score. The number of clusters in CC3 and PHH3 channels (number of cells with positive signals) are found by the same clustering algorithm with the optimal cluster size obtained in the DAPI channel.

Quantification of follicle growth. Follicle diameters D were measured by taking the average of the major and minor axes from the Fit Ellipse

tool in ImageJ. Growth rate $G(r)$ of follicles was defined as the change of diameter dD over a period of time dt, normalised by the diameter: $G(r) = \frac{dD(t)}{D(t)dt}$, which is equivalent to $d\ln D(t)/dt$ when dt is small. For microtissues, we drew four diameters across each follicle to get the mean follicle diameter in each day, In practice, we calculated the growth rate, $G(r)$, of a follicle with diameter D at time t from the discrete time evolution as:

$$G(r) = (\ln(D(t)) - \ln(D(t - \Delta T))/\Delta T, \quad (5)$$

where ΔT is the time interval between two consecutive time points and ΔT is usually 1 day or 2 days. The growth rate for diameters >180 μm was used to plot G(r) at the maturation phase.

Statistical analysis

No statistical method was used to predetermine the sample size. Sample sizes were determined based on previous studies in similar fields. All graphs and statistical tests were created using Origin 2021b. Statistical significance for two-group comparisons was determined using the two-tailed Mann-Whitney U test or the one-sample T-test (wherever mentioned in the legend). Boxplots show the mean (star), median (centre line), quartiles (box limits) and 1.5x interquartile range (whiskers). Sample sizes (n value) of independent experiments are indicated in figure legends. Data collection and analysis were not performed blinded to the conditions of the experiments, and no data were excluded from the analyses. No specific methods were used for random allocation of samples into groups. All experiments were performed on at least four biological replicates. Bar plots are presented as arithmetic mean ± standard deviation. All images are representative of at least three independent experiments.

Reporting summary

Further information on research design is available in the Nature Portfolio Reporting Summary linked to this article.

Data availability

The RNA-seq data have been deposited in the NCBI GEO repository with the accession code GSE309281. The rest of the data generated or analyzed during this study are all included in the published article and its Supplementary Information files. Source data are provided with this paper. All other data are available from the corresponding authors upon reasonable request. Source data are provided with this paper.

Code availability

All scripts newly written in this study can be accessed via Zenodo[72] at https://doi.org/10.5281/zenodo.17174104.

References

1. McNatty, P. et al. Control of early ovarian follicular development. *J. Reprod. Fertil. Suppl.* **54**, 3–16 (1999).
2. Edson, M. A., Nagaraja, A. K., Matzuk, M. M. & Genetics, H. The mammalian ovary from genesis to revelation. *Endocr. Rev.* **30**, 624–712 (2009).
3. Hertig, A. T. & Adams, E. C. Studies on the human oocyte and its follicle. I. Ultrastructural and histochemical observations on the primordial follicle stage. *J. Cell Biol.* **34**, 647–675 (1967).
4. França, M. M. & Mendonca, B. B. Genetics of ovarian insufficiency and defects of folliculogenesis. *Best. Pr. Res Clin. Endocrinol. Metab.* **36**, 101594 (2022).
5. Pascoletti, G. et al. Dynamic characterization of the biomechanical behaviour of bovine ovarian cortical tissue and its short-term effect on ovarian tissue and follicles. *Materials* **13**, 3759 (2020).
6. Shah, J. S. et al. Biomechanics and mechanical signaling in the ovary: a systematic review. *J. Assist Reprod. Genet* **35**, 1135 (2018).
7. Sun, C., Yang, X., Wang, T., Cheng, M. & Han, Y. Ovarian Biomechanics: From Health to Disease. *Front Oncol.* **11**, 744257 (2021).
8. Hornick, J. E., Duncan, F. E., Shea, L. D. & Woodruff, T. K. Isolated primate primordial follicles require a rigid physical environment to survive and grow in vitro. *Hum. Reprod.* **27**, 1801 (2012).
9. Pietroforte, S., Plough, M. & Amargant, F. Age-associated increased stiffness of the ovarian microenvironment impairs follicle development and oocyte quality and rapidly alters follicle gene expression. Preprint at https://doi.org/10.1101/2024.06.09.598134 (2024).
10. Cheng, Y. et al. Actin polymerization-enhancing drugs promote ovarian follicle growth mediated by the Hippo signaling effector YAP. *FASEB J.* **29**, 2423 (2015).
11. Kawamura, K. et al. Hippo signaling disruption and Akt stimulation of ovarian follicles for infertility treatment. *Proc. Natl Acad. Sci. USA* **110**, 17474–17479 (2013).
12. Borreguero-Muñoz, N. et al. The Hippo pathway integrates PI3K–Akt signals with mechanical and polarity cues to control tissue growth. *PLoS Biol.* **17**, e3000509 (2019).
13. Nagamatsu, G., Shimamoto, S., Hamazaki, N., Nishimura, Y. & Hayashi, K. Mechanical stress accompanied with nuclear rotation is involved in the dormant state of mouse oocytes. *Sci. Adv.* **5**, eaav9960 (2019).
14. Amargant, F. et al. Ovarian stiffness increases with age in the mammalian ovary and depends on collagen and hyaluronan matrices. *Aging Cell* **19**, e13259 (2020).
15. Mara, J. N. et al. Ovulation and ovarian wound healing are impaired with advanced reproductive age. *Aging* **12**, 9686–9713 (2020).
16. Delarue, M. et al. Compressive stress inhibits proliferation in tumor spheroids through a volume limitation. *Biophysj* **107**, 1821–1828 (2014).
17. Barbazan, J. et al. Cancer-associated fibroblasts actively compress cancer cells and modulate mechanotransduction. *Nat. Commun.* **14**, 6966 (2023).
18. Li, P. et al. N-Cadherin-Mediated Activation of PI3K/Akt-GSK-3β Signaling Attenuates Nucleus Pulposus Cell Apoptosis Under High-Magnitude Compression. *Cell Physiol. Biochem* **44**, 229–239 (2017).
19. Villeneuve, C. et al. Mechanical forces across compartments coordinate cell shape and fate transitions to generate tissue architecture. *Nat. Cell Biol.* **26**, 207–218 (2024).
20. Shroff, N. P. et al. Proliferation-driven mechanical compression induces signalling centre formation during mammalian organ development. *Nat. Cell Bio.* **26**, 519–529 (2024).
21. Chan, C. J., Bevilacqua, C. & Prevedel, R. Mechanical mapping of mammalian follicle development using Brillouin microscopy. *Commun. Biol.* **4**, 1133 (2021).
22. Young, J. M. & McNeilly, A. S. Theca: the forgotten cell of the ovarian follicle. *Reproduction* **140**, 489–504 (2010).
23. Roberts, A. J. & Skinner, M. K. Mesenchymal-epithelial cell interactions in the ovary: estrogen-induced theca cell steroidogenesis. *Mol. Cell Endocrinol.* **72**, R1–R5 (1990).
24. Stein, I. F. & Leventhal, M. L. Amenorrhea associated with bilateral polycystic ovaries. *Am. J. Obstet. Gynecol.* **29**, 181–191 (1935).
25. Candelaria, N. R. & Richards, J. S. Targeted deletion of NR2F2 and VCAM1 in theca cells impacts ovarian follicular development: insights into polycystic ovary syndrome?. *Biol. Reprod.* **110**, 782 (2024).
26. Melo, A. S., Ferriani, R. A. & Navarro, P. A. Treatment of infertility in women with polycystic ovary syndrome: approach to clinical practice. *Clinics* **70**, 765 (2015).
27. Geist, S. H. & Gaines, J. A. Diffuse luteinization of the ovaries associated with the masculinization syndrome. *Am. J. Obstet. Gynecol.* **43**, 975–983 (1942).
28. Meczekalski, B. et al. Hyperthecosis: an underestimated non-tumorous cause of hyperandrogenism. *Gynecol. Endocrinol.* **37**, 677–682 (2021).

29. Rodgers, R. J. & Laven, J. S. E. Genetic relationships between early menopause and the behaviour of theca interna during follicular atresia. *Human Reprod.* **35**, 2185–2187 (2020).
30. Thomas, C., Marx, T. L., Penir, S. M. & Schuh, M. Ex vivo imaging reveals the spatiotemporal control of ovulation. *Nat. Cell Biol.* **26**, 1997–2008 (2024).
31. Knight, P. G. & Glister, C. Theca cells and the regulation of ovarian androgen production. *Biosci. Proc.* **8**, 295–310 (2019).
32. Kogure, Y. S. et al. Admp regulates tail bending by controlling ventral epidermal cell polarity via phosphorylated myosin localization in Ciona. *Dev. (Camb.)* **149**, dev200215 (2022).
33. Emery, A. et al. N-cadherin mechanosensing in ovarian follicles controls oocyte maturation and ovulation. *Elife* **13**, RP92068 (2025).
34. Mora, J. M. et al. Characterization and significance of adhesion and junction-related proteins in mouse ovarian follicles. *Biol. Reprod.* **86**, 1–14 (2012).
35. Chan, C. J. et al. Hydraulic control of mammalian embryo size and cell fate. *Nature* **571**, 112–116 (2019).
36. Tingen, C. M. et al. A macrophage and theca cell-enriched stromal cell population influences growth and survival of immature murine follicles in vitro. *Reproduction* **141**, 809 (2011).
37. Sangha, G. K. & Guraya, S. S. Histochemical changes in acid and alkaline phosphatase activities in the growing follicles and corpora lutea of the rat ovary. *Acta Morphol. Neerl. Scand.* **26**, 43–49 (1988).
38. He, C. et al. Quantifying the compressive force of 3d cardiac tissues via calculating the volumetric deformation of built-in elastic gelatin microspheres. *Adv. Health. Mater.* **10**, 2001716 (2021).
39. Heeren, A. M. et al. Development of the follicular basement membrane during human gametogenesis and early folliculogenesis. *BMC Dev. Biol.* **15**, 4 (2015).
40. Akkoyunlu, G., Demir, R. & Üstünel, Ï Distribution patterns of TGF-α, laminin and fibronectin and their relationship with folliculogenesis in rat ovary. *Acta Histochem* **105**, 295–301 (2003).
41. Wulff, C., Wilson, H., Wiegand, S. J., Rudge, J. S. & Fraser, H. M. Prevention of thecal angiogenesis, antral follicular growth, and ovulation in the primate by treatment with vascular endothelial growth factor trap R1R2. *Endocrinology* **143**, 2797–2807 (2002).
42. Taylor, P. D., Hillier, S. G. & Fraser, H. M. Effects of GnRH antagonist treatment on follicular development and angiogenesis in the primate ovary. *J. Endocrinol.* **183**, 1–17 (2004).
43. De Candia, L. M. & Rodgers, R. J. Characterization of the expression of the alternative splicing of the ED-A, ED-B and V regions of fibronectin mRNA in bovine ovarian follicles and corpora lutea. *Reprod. Fertil. Dev.* **11**, 367–377 (1999).
44. Hunter, M. C. et al. Hsp90 binds directly to fibronectin (fn) and inhibition reduces the extracellular fibronectin matrix in breast cancer cells. *PLoS One* **9**, e86842 (2014).
45. Boel, N. M. E., Hunter, M. C. & Edkins, A. L. LRP1 is required for novobiocin-mediated fibronectin turnover. *Sci. Rep.* **8**, 1–14 (2018).
46. Puts, R. et al. Functional regulation of YAP mechanosensitive transcriptional coactivator by Focused Low-Intensity Pulsed Ultrasound (FLIPUS) enhances proliferation of murine mesenchymal precursors. *PLoS One* **13**, e0206041 (2018).
47. El-Hayek, S., Yang, Q., Abbassi, L., FitzHarris, G. & Clarke, H. J. Mammalian oocytes locally remodel follicular architecture to provide the foundation for germ line-soma communication. *Curr. Biol.* **28**, 1124 (2018).
48. Töpfer, U., Santillán, K. Y. G., Fischer-Friedrich, E. & Dahmann, C. Distinct contributions of ECM proteins to basement membrane mechanical properties in Drosophila. *Dev. (Camb.)* **149**, dev200456 (2022).
49. Lamiré, L. A. et al. Gradient in cytoplasmic pressure in germline cells controls overlying epithelial cell morphogenesis. *PLoS Biol.* **18**, e3000940 (2020).
50. R, D. L. F. & JJ, E. Transcriptional activity of the mouse oocyte genome: companion granulosa cells modulate transcription and chromatin remodeling. *Dev. Biol.* **229**, 224–236 (2001).
51. Irving-Rodgers, H. F. & Rodgers, R. J. Extracellular matrix in ovarian follicular development and disease. *Cell Tissue Res* **322**, 89–98 (2005).
52. Espey, L. L. Ovarian contractility and its relationship to ovulation: A review. *Biol. Reprod.* **19**, 540–551 (1978).
53. Jaeschke, A., Hepburn, M. S., Mowla, A., Kennedy, B. F. & Chan, C. J. Three-dimensional quantitative micro-elastography reveals alterations in spatial elasticity patterns in murine ovaries during ageing. *Commun. Biol.* **8**, 1409 (2025).
54. Winklbauer, R. & Stoltz, C. Fibronectin fibril growth in the extracellular matrix of the Xenopus embryo. *J. Cell Sci.* **108**, 1575–1586 (1995).
55. Ferraro, R., Guido, S., Caserta, S. & Tassieri, M. i-Rheo-optical assay: Measuring the viscoelastic properties of multicellular spheroids. *Mater. Today Bio* **26**, 101066 (2024).
56. Dolega, M. E. et al. Cell-like pressure sensors reveal increase of mechanical stress towards the core of multicellular spheroids under compression. *Nat. Commun.* **8**, 1–9 (2017).
57. Varelas, X. et al. The Crumbs Complex Couples Cell Density Sensing to Hippo-Dependent Control of the TGF-b-SMAD Pathway. *Developmental Cell* **19**, 831–844 (2010).
58. Cai, H. & Xu, Y. The role of LPA and YAP signaling in long-term migration of human ovarian cancer cells. *Cell Commun. Signal.* **11**, 1–13 (2013).
59. Dolega, M. E. et al. Extracellular matrix in multicellular aggregates acts as a pressure sensor controlling cell proliferation and motility. *Elife* **10**, e63258 (2021).
60. Simon, A. M., Goodenough, D. A., Li, E. & Paul, D. L. Female infertility in mice lacking connexin 37. *Nature* **385**, 525–529 (1997).
61. Richard, S., Zhou, Y., Jasoni, C. L. & Pankhurst, M. W. Ovarian follicle size or growth rate can both be determinants of ovulatory follicle selection in mice. *Biol. Reprod.* **110**, 127–136 (2024).
62. Vian, A. et al. In situ quantification of osmotic pressure within living embryonic tissues. *Nat. Commun.* **14**, 7023 (2023).
63. Tse, J. M. et al. Mechanical compression drives cancer cells toward invasive phenotype. *Proc. Natl Acad. Sci. USA* **109**, 911–916 (2012).
64. Wang, H. Y. et al. Rejuvenation of aged oocyte through exposure to young follicular microenvironment. *Nat. Aging* **4**, 1194–1210 (2024).
65. Umehara, T. et al. Female reproductive life span is extended by targeted removal of fibrotic collagen from the mouse ovary. *Sci. Adv.* **8**, 4564 (2022).
66. Monnier, S. et al. Effect of an osmotic stress on multicellular aggregates. *Methods* **94**, 114–119 (2016).
67. Huang, C.-K., Yong, X., She, D. T. & Lim, C. T. Surface curvature and basal hydraulic stress induce spatial bias in cell extrusion. *Elife* **12**, RP84921 (2024).
68. DI Tommaso, P. et al. Nextflow enables reproducible computational workflows. *Nat. Biotechnol.* **35**, 316–319 (2017).
69. Love, M. I., Huber, W. & Anders, S. Moderated estimation of fold change and dispersion for RNA-seq data with DESeq2. *Genome Biol.* **15**, 550 (2014).
70. Couturier, E., Vella, D. & Boudaoud, A. Compression of a pressurized spherical shell by a spherical or flat probe. *Eur. Phys. J. E* **45**, 1–6 (2022).
71. Vella, D., Ajdari, A., Vaziri, A. & Boudaoud, A. The indentation of pressurized elastic shells: From polymeric capsules to yeast cells. *J. R. Soc. Interface* **9**, 448–455 (2012).
72. Chan, C. J., Biswas, A. & Lou, Y. Surface mechanics and compressive stress impact mammalian follicle development. *Zenodo* https://doi.org/10.5281/zenodo.17174105 (2025).

Acknowledgements
We thank Apoorva Shivankar for preliminary experiments on tissue staining in aged mouse ovaries. We are grateful to Jin Zhu for his detailed discussions on the RNA sequencing data; Brenda Nai Mui Hoon and Chwee Teck Lim for training and usage of atomic force microscopy; Xianbin Yong and Cheng Kuang Huang for assistance in traction force microscopy; Aaron Farrugia for providing Novobiocin; and the lab of Krystyn Van Vliet for providing the gelatin beads. We thank Jacques Prost for discussions on interpreting AFM data. We thank the MBI Wet Lab Core for facility and technical support, the Singapore Microscopy and Bioimaging Analysis (SiMBA, MBI) core for microscopy, the Microfabrication core for help with the microwells, and the High-throughput Molecular Genetics (HMG, MBI) core for RNA-seq support. The Chan lab is supported by the Ministry of Education under the Research Centres of Excellence programme through the Mechanobiology Institute and the Department of Biological Sciences at the National University of Singapore, the Ministry of Education Tier2 grant (T2EP30222-0026), National Research Foundation Mid-size Grant (NRF-MSG-2023-0001) and the Bia-Echo Asia Centre for Reproductive Longevity and Equality (ACRLE) at the National University of Singapore. C.J.C. acknowledges the support of the Singaporean Teaching and Academic Research Talent Inauguration Grant (START). We thank Raymond Rodgers, Tetsuya Hiraiwa, and Yuchen Long for providing valuable feedback on our manuscript.

Author contributions
Conceptualization: A.B, C.J.C.; Investigation: A.B., B.H.N., K.T., S.D., Z.W., K.W.L., T.B.L., X.T., C.J.C.; Formal Analysis: A.B., Y.L., K.T., C.J.C; Resources: Y.T., I.B.; Writing: A.B., C.J.C; Funding Acquisition: C.J.C.; Supervision: C.J.C.

Competing interests
The authors declare no competing interests.

Additional information
Supplementary information The online version contains supplementary material available at https://doi.org/10.1038/s41467-025-65390-y.

Correspondence and requests for materials should be addressed to Chii Jou Chan.

Peer review information *Nature Communications* thanks Christiani Andrade Amorim and the other anonymous reviewer(s) for their contribution to the peer review of this work. A peer review file is available.